

RESEARCH ARTICLE

WILEY

An accurate and robust HLLC-type Riemann solver for the compressible Euler system at various Mach numbers

Wenjia Xie^{id} | Ran Zhang | Jianqi Lai | Hua Li

College of Aerospace Science and Engineering, National University of Defense Technology, Hunan, China

Correspondence

Wenjia Xie, College of Aerospace Science and Engineering, National University of Defense Technology, Hunan 410073, China.
Email: xiewenjia@nudt.edu.cn

Funding information

National Natural Science Foundation of China, Grant/Award Number: 11472004; Foundation of Innovation of National University of Defense Technology, Grant/Award Number: B150106

Summary

A simple, robust, and accurate HLLC-type Riemann solver for the compressible Euler equations at various Mach numbers is built. To cure shock instability of the HLLC solver at strong shocks, a pressure-control technique, which plays a role in limiting the propagation of erroneous pressure perturbation, is proposed. With an all Mach correction method for the compressible Euler system, the proposed method is further extended to compute flow problems at low Mach numbers. The proposed all Mach HLLC-type scheme has been implemented and used to compute a variety of flow problems ranging from hypersonic compressible to low Mach incompressible flow regimes. Various numerical results demonstrate that the obtained all Mach HLLC-type scheme is both accurate and stable for all speed ranges.

KEYWORDS

Euler equations, finite volume schemes, HLLC scheme, hypersonic, low Mach number, numerical shock instability

1 | INTRODUCTION

Godunov-type Riemann solvers as among the most popular shock-capturing schemes have been widely used in computational fluid dynamics. Due to their clear physical interpretations, Godunov-type schemes play a fundamental role in simulating compressible flows at moderate Mach numbers. In some applications, it is sometimes essential to take into account weakly compressible flow phenomena even when a flow is at the high Mach regime. This requires that numerical methods should capture shock waves stably in high speed flows and simulate flows accurately at low Mach numbers.

The HLLC approximate Riemann solver¹ is one of the most popular flux functions to solve Euler equations. Like Roe-type² and Osher-type schemes,³ the HLLC flux is able to resolve contact and shear waves with minimal diffusion. Furthermore, the scheme is based on the famous HLL Riemann solver⁴; therefore, it can resolve isolated shock exactly with certain wave speed estimates. The HLLC scheme also satisfies the entropy condition and preserves positivity. Due to its desirable features, the HLLC approach has been studied and applied extensively in both academic and engineering communities. It has also been extended to other applications such as turbulent flows,⁵ MHD equations^{6,7} and multiphase flows.^{8,9} However, the HLLC scheme suffers from numerical shock anomalies such as the carbuncle phenomenon and the postshock oscillations, which limit its application to hypersonic flow computations. Since its discovery by Peery and Imlay,¹⁰ the carbuncle phenomenon has been perhaps the most famous unresolved deficiency of Godunov-type methods. Quirk¹¹ first conducted a systematic analysis of the unfavorable pathologies of Godunov-type schemes for flows at high Mach numbers. He found that dissipative numerical fluxes, which smeared contact and shear waves severely, were endowed with high resistance against shock anomalies. Consequently, he suggested to hybridize a low dissipative scheme

(eg, the Roe scheme²) with a dissipative one (eg, the HLLC scheme¹²) to circumvent the instability problem without compromising the high resolution of the numerical flux. In the same spirit of Quirk's technique, various hybrid solvers were developed and implemented in numerical codes to compute flow problems. To improve the robustness of the HLLC scheme, Kim et al¹³ proposed a hybrid method that combined the HLLC and HLL schemes in a single framework by a switching function. The instabilities were prevented by the numerical dissipation of the HLL scheme, which was activated in the vicinity of strong shocks. Similar cures for the shock instability of the HLLC scheme were followed in other works.¹⁴⁻¹⁷ Shen et al¹⁸ conducted a stability analysis of hybrid schemes to cure shock instability. They argued that the scheme with shear viscosity was quite robust against strong shocks. To eliminate the shock instability of the HLLC scheme, they also used a hybrid technique which combined the HLLC with a shear dissipative HLLC-type solver (ie, the HLLCM scheme¹⁹). Recently, Rodionov²⁰ proposed a new approach for curing the carbuncle instability. Contrasting to the hybrid methods which rely on numerical dissipation inherent in schemes themselves, Rodionov's approach introduced artificial viscosity terms in the form of right-hand sides of the Navier-Stokes equations to smear shear waves in the shock layer only. Thus, the method is general and can be applied to cure the shock instability of a large variety of shock-capturing schemes. Although introducing additional numerical dissipation or artificial viscosity has been well demonstrated to be effective to eliminate the shock instability, there are still some issues need to address with caution. For example, the increased numerical dissipation will probably contaminate computational domain that is away from the shock region. Thus, it is still attractive to propose a cure for suppressing the shock instability without resorting to numerical dissipation corresponding to contact or shear waves. In the current study, we apply a pressure-control technique to improve the robustness of the HLLC scheme in the vicinity of strong shocks. The essence of this technique is to limit the propagation of erroneous pressure perturbation from inside the numerical shock structure to the downstream region. The rationality of this modification comes from the observation in the work of Xie et al²¹ that, if the mass flux across the normal shock is correctly preserved (ie, $(\rho u)_R = (\rho u)_L$, L, R represent left and right states across the shock), the instability can be suppressed successfully. One desirable feature of the technique is that it does not introduce additional numerical dissipation on contact or shear waves because only a pressure dissipative term is added to the inviscid flux. In the boundary layer, pressure is usually constant normal to the wall, thus the pressure dissipative term plays a negligible role there and the high resolution of the HLLC solver is preserved.

It is well known that Godunov-type schemes fail to be accurate at low Mach numbers in most cases.²² Like other Godunov-type schemes such as Roe² or HLLC,¹² the HLLC scheme also cannot guarantee the correct asymptotic behavior at low Mach numbers, which makes it unsuitable for the accurate simulation of weakly compressible flow structures. Guillard et al^{23,24} presented a series of asymptotic analysis of Godunov-type schemes in the low Mach number regime, they exhibited that the solutions computed by the discrete scheme contained pressure fluctuations of order of the Mach number while the physical pressure scaled with the square of the Mach number. They rescaled the Roe scheme in low Mach number flow regions by modifying the numerical dissipation with a preconditioned approach.^{23,25,26} Li and Gu introduced the all-speed Roe scheme in a series of works.²⁷⁻²⁹ Unlike the Roe-Turkel scheme proposed by Guillard and Viozat²³ which modified both the eigenvalues and eigenvectors of the numerical dissipation, the all-speed Roe scheme only modified the nonlinear eigenvalues. Rieper³⁰ also proposed a low Mach number fix for Roe scheme, the remedy was based on the observation in the works of Thornber et al³¹ and Rieper and Bader³² that the unphysical behavior in low Mach numbers was related to the velocity jump normal to the cell interface. Dellacherie et al^{33,34} defined and analyzed the low Mach number problem through a linear analysis of a perturbed linear wave equation. They found that the profound root of the low Mach number problem was linear. An all Mach correction was proposed to cure the Godunov scheme for the linear wave equation, which was further extended to nonlinear cases including the barotropic Euler system and the full Euler compressible system. Furthermore, the theoretical framework of Dellacherie et al also justified other existing all Mach schemes, for example, the mentioned preconditioning methods of Guillard and Viozat,²³ Rieper's LMRoe scheme,³⁰ and other similar approaches.³⁵⁻³⁷

Although the low Mach number corrections for Godunov-type schemes are diverse, little attention has been devoted to the low Mach number problem of the HLLC scheme. It was expected in the work of Rieper³⁰ that the low Mach number fix for Roe's method can be applied to other Godunov-type schemes including the HLLC approximate Riemann solver, but the extension was not straightforward due to the nonlinear formulations of its flux function. To the best knowledge of authors, Luo et al³⁸ were the first to modify and extend the HLLC scheme to compute the flows at all speeds. They proposed a modification of the signal velocities in the HLLC scheme based on the eigenvalues of the preconditioned Euler equations to reduce excessive numerical diffusion at the low Mach number. A similar approach was also used by Gupta et al^{39,40} to improve the HLLC scheme for multiphase flow simulations at low Mach numbers. Pelanti⁴¹ also developed a low Mach number correction for the HLLC-type method. By defining a novel reformulation of the HLLC solver, the author succeeded

to extend the methodology of the preconditioned Roe-Turkel scheme of Guillard-Viozat for the Euler equations²³ to the HLLC-type method for the two-phase flow model. However, these modified HLLC schemes cannot capture strong shocks stably in hypersonic regime. In this paper, we propose a much simpler low Mach correction for the HLLC-type method, thanks to the innovative work of Dellacherie et al.^{33,34} Our new accurate and robust HLLC-type Riemann solver has several advantages over other methods: It is able to simulate flows where compressible and weakly compressible flow regimes coexist in the domain of interest. It is endowed with high level of robustness against strong shocks. For other low Mach schemes, they are often not free from the instability problems in hypersonic flows. Moreover, the new scheme preserves the simple formulation of the HLLC scheme, thus it will take only few minutes to implementing the correction into the existing codes of compressible solvers.

The outline of the rest of this paper is as follows. In Section 2, governing equations of compressible flows and their related finite volume discretization are presented. We also review the HLLC approximate Riemann solver in the same section. In Section 3, a modified HLLC-type scheme with improved robustness against strong shocks is presented. A matrix instability analysis is also included to demonstrate its robustness at shocks. In Section 4, we introduce a simple low Mach number improvement for the HLLC-type scheme. A discrete asymptotic analysis of the HLLC-type scheme is also included. In Section 5, the desirable properties of the proposed scheme are discussed. The accuracy and robustness of the proposed method are tested in Section 6. Finally, concluding remarks are made in Section 7.

2 | GOVERNING EQUATIONS AND FINITE VOLUME DISCRETIZATION

The two-dimensional (2D) Euler equations may be written in integral form as

$$\frac{\partial}{\partial t} \int_{\Omega} \mathbf{U} d\Omega + \oint_{\partial\Omega} \mathbf{F} dS = 0, \quad (1)$$

where $\partial\Omega$ denote boundaries of the control volume Ω . The state vector and flux vector are defined as

$$\mathbf{U} = \begin{bmatrix} \rho \\ \rho u \\ \rho v \\ \rho e \end{bmatrix}, \quad \mathbf{F} = \begin{bmatrix} \rho q \\ \rho u q + p n_x \\ \rho v q + p n_y \\ (\rho e + p) q \end{bmatrix}, \quad (2)$$

where ρ , e , and p represent density, specific total energy, and pressure respectively, and $\mathbf{u} = (u, v)$ is the flow velocity. The directed velocity, $q = u n_x + v n_y$, is the component of velocity acting in the \mathbf{n} direction, where $\mathbf{n} = [n_x, n_y]^T$ is the outward unit vector normal to the surface element dS . The equation of state is in the form

$$p = (\gamma - 1) \rho \left[e - \frac{1}{2} (u^2 + v^2) \right], \quad (3)$$

where γ is the specific heat ratio. We consider discretizing system (1) with a cell-centered finite-volume method over a 2D domain subdivided into some structured quadrilateral cells. The semidiscrete finite volume scheme over a particular control volume Ω_i can be written as

$$\frac{d\mathbf{U}_i}{dt} + \frac{1}{|\Omega_i|} \sum_{\Gamma_{ij} \subset \partial\Omega_i} |\Gamma_{ij}| \Phi_{ij} = 0. \quad (4)$$

In the above expression, \mathbf{U}_i is the cell average of \mathbf{U} on Ω_i , $|\Omega_i|$ denotes the volume of Ω_i . Γ_{ij} denotes the common edge of two neighboring cells Ω_i , and Ω_j , \mathbf{n}_{ij} represents the unit vector normal to Γ_{ij} pointing from Ω_i to Ω_j and $|\Gamma_{ij}|$ is the length of face Γ_{ij} . The flux Φ_{ij} is the calculated numerical flux that is supposed to be constant along the individual face Γ_{ij} .

2.1 | The HLLC approximate Riemann solver

The HLLC Riemann solver¹ is one of the most popular approaches to solve the Riemann problem approximately. It can be considered to be a modification of the HLL scheme⁴ whereby the missing contact and shear waves in the Euler equations are restored. With a suitable choice of the contact and acoustic wave speeds, the HLLC scheme is able to resolve both isolated shock and contact waves exactly, and furthermore, it is also positively conservative and does not admit an entropy violating jump in the expansion region where the flow becomes sonic. In Figure 1, the wave structure of the HLLC solver

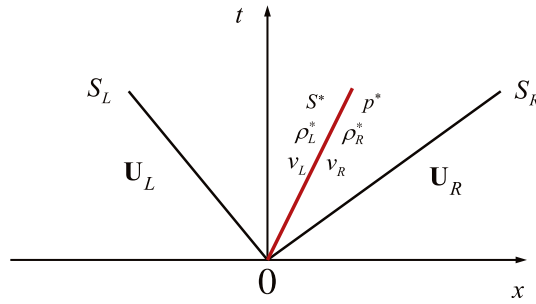


FIGURE 1 Wave structure of the HLLC approximate Riemann solver [Colour figure can be viewed at wileyonlinelibrary.com]

is illustrated. As shown, solution of the Riemann problem is approximated by four constant states separated by three waves emerging from the initial discontinuity at the interface, they are defined as

$$\mathbf{U}_{\text{HLLC}} = \begin{cases} \mathbf{U}_L, & 0 \leq S_L \\ \mathbf{U}_L^*, & S_L \leq 0 \leq S^* \\ \mathbf{U}_R^*, & S^* \leq 0 \leq S_R \\ \mathbf{U}_R, & 0 \geq S_R, \end{cases} \quad (5)$$

where \mathbf{U}_L^* and \mathbf{U}_R^* represent intermediate states at the left and right sides of the contact discontinuity respectively,

$$\mathbf{U}_K^* = [\rho_K^*, \rho_K^* u_K^*, \rho_K^* v_K^*, \rho_K^* e_K^*], \quad K = L, R, \quad (6)$$

and S_L, S_R denote the left and right wave speeds. The corresponding interface flux, denoted by Φ_{HLLC} , is defined as

$$\Phi_{\text{HLLC}} = \begin{cases} \mathbf{F}_L, & \text{if } 0 \leq S_L, \\ \mathbf{F}_L^*, & \text{if } S_L \leq 0 \leq S^*, \\ \mathbf{F}_R^*, & \text{if } S^* \leq 0 \leq S_R, \\ \mathbf{F}_R, & \text{if } 0 \geq S_R. \end{cases} \quad (7)$$

To determine the intermediate fluxes \mathbf{F}_L^* and \mathbf{F}_R^* , one need to consider the following Rankine-Hugoniot conditions across each of the waves of speeds S_L, S^* and S_R :

$$\begin{aligned} \mathbf{F}_L^* &= \mathbf{F}_L + S_L (\mathbf{U}_L^* - \mathbf{U}_L) \\ \mathbf{F}_R^* &= \mathbf{F}_L^* + S^* (\mathbf{U}_R^* - \mathbf{U}_L^*) \\ \mathbf{F}_R^* &= \mathbf{F}_R + S_R (\mathbf{U}_R^* - \mathbf{U}_R). \end{aligned} \quad (8)$$

By jump conditions (8), the intermediate states in the star region can be derived as

$$\begin{aligned} \rho_K^* &= \frac{\alpha_K}{S_K - S^*} \\ u_K^* &= u_K + n_x (S^* - q_K) \\ v_K^* &= v_K + n_y (S^* - q_K) \\ e_K^* &= e_K + (S^* - q_K) / (S^* + p_K / \alpha_K), \end{aligned} \quad (9)$$

where the contact velocity and pressure in the star region can be obtained by

$$\begin{aligned} S^* &= \frac{\alpha_R q_R - \alpha_L q_L + p_L - p_R}{\alpha_R - \alpha_L} \\ p^* &= \frac{\alpha_R p_L - \alpha_L p_R - \alpha_L \alpha_R (q_L - q_R)}{\alpha_R - \alpha_L}. \end{aligned} \quad (10)$$

In Equation (9) and Equation (10), we use the following simple notations that are defined by Shen et al¹⁹:

$$\alpha_L = \rho_L (S_L - q_L), \quad \alpha_R = \rho_R (S_R - q_R). \quad (11)$$

According to Toro,⁴² the numerical flux in (7) can be rewritten in an alternative form as

$$\Phi_{\text{HLLC}} = \begin{cases} \mathbf{U}_L q_L + \mathbf{D}_L, & \text{if } 0 \leq S_L, \\ \mathbf{U}_L^* S^* + \mathbf{D}^*, & \text{if } S_L \leq 0 \leq S^*, \\ \mathbf{U}_R^* S^* + \mathbf{D}^*, & \text{if } S^* \leq 0 \leq S_R, \\ \mathbf{U}_R q_R + \mathbf{D}_R, & \text{if } 0 \geq S_R, \end{cases} \quad (12)$$

where $\mathbf{D}_K = p_K(0, n_x, n_y, u_K)^T$ for $K = L, R$ and $\mathbf{D}^* = p^*(0, n_x, n_y, S^*)$. To complete the HLLC Riemann solver, an algorithm to compute the wave speeds S_L and S_R must be given. Here, we use a simple estimate proposed by Davis⁴³

$$S_L = \min(q_L - c_L, q_R - c_R), \quad S_R = \max(q_L + c_L, q_R + c_R), \quad (13)$$

where c_L and c_R are the sound speeds of the left and right states. Another commonly used estimate is due to Einfeldt et al⁴⁴

$$S_L = \min(q_L - c_L, \hat{q} - \hat{c}), \quad S_R = \max(q_R + c_R, \hat{q} + \hat{c}). \quad (14)$$

3 | REMEDY FOR NUMERICAL SHOCK INSTABILITY

In this section, we derive a shock-stable enhanced HLLC-type scheme denoted as HLLC-P (HLLC scheme with a Pressure-control technique). In contrast to the original HLLC scheme which is vulnerable to numerical shock instability at strong shocks, this modified scheme is able to capture shocks stably without any shock anomalies. The modification is inspired by a recent study on numerical instabilities of Godunov-type schemes for strong shocks which is presented in the work of Xie et al.²¹ To validate the effectiveness of the pressure-control technique at shocks, we carry out a matrix stability analysis of these HLLC-type schemes. This analysis is commonly used to determine whether a numerical scheme is shock-stable or not.

3.1 | A shock-stable HLLC-type scheme

In a recent work, Xie et al²¹ have carried out a series of numerical investigations of numerical instability of Godunov-type schemes. They found that the numerical shock instability originated from the intermediate states inside the shock structure where perturbation errors were generated and propagated downstream. Thus, in order to suppress the shock instability, a possible way is to damp the perturbation errors and limit their propagation downstream. Here, we add a pressure dissipative term to the original HLLC scheme similar to the antidiffusion term used in the HLLEM flux proposed by Einfeldt.¹² The resulting numerical flux function can be written by

$$\Phi_{\text{HLLC-P}} = \Phi_{\text{HLLC}} + \Phi_p, \quad (15)$$

where the added pressure dissipative term is defined as

$$\Phi_p = (f - 1) \frac{S_L S_R}{S_R - S_L} \frac{1}{1 + |\hat{M}|} \frac{\Delta p}{\hat{c}^2} \begin{pmatrix} 1 \\ \hat{u} \\ \hat{v} \\ \frac{1}{2} \hat{q}^2 \end{pmatrix}. \quad (16)$$

In Equation (16), S_L and S_R are defined in Equations (13) or (14), Δp represents pressure difference, \hat{M} , \hat{c} , \hat{u} , \hat{v} , and \hat{q} denote Mach number, sound speed, velocity components, and normal velocity evaluated by Roe averaged method at the interface respectively. f represents a pressure weight function, it is defined as

$$f = \min(f_{p,i,j+1/2}, f_{p,i-1/2,j}, f_{p,i-1/2,j+1}, f_{p,i+1/2,j}, f_{p,i+1/2,j+1})^3, \quad (17)$$

with

$$f_p = \min(p_R/p_L, p_L/p_R). \quad (18)$$

It can be observed from Equations (17) and (18) that the correction term on the right of Equation (15) is only activated in the vicinity of shocks, and in the smooth region, f approaches unit and the HLLC-P scheme turns into the HLLC solver. The

pressure dissipative term introduced in Equation (16) plays a part in damping erroneous pressure perturbation generated inside the numerical shock structure and helping stabilize the shock.

3.2 | A matrix stability analysis of the HLLC-type schemes

In order to determine whether the pressure-control technique is effective in eliminating numerical shock instability, we conduct a matrix stability analysis to study numerical behaviors of HLLC-type schemes at shocks. This analysis approach is first proposed by Dumbser et al.⁴⁵ and followed by many scholars^{18,46-48} to study the occurrence of unstable modes during the shock wave computation. A significant advantage of this method is that it is able to quantitatively reveal the shock stability mechanism of numerical flux. For self-containedness, we describe the approach once more and readers are referred to references^{18,45} for more details.

For the stability analysis of a steady field, we assume that the domain is submitted to small numerical random errors as

$$\mathbf{U}_i = \mathbf{U}_i^0 + \delta \mathbf{U}_i, \quad (19)$$

where \mathbf{U}_i^0 is the steady mean value and $\delta \mathbf{U}_i$ represents the small numerical random perturbation. The flux function can be linearized around the steady mean value as follows:

$$\Phi_{ij}(\mathbf{U}_i, \mathbf{U}_j) = \Phi_{ij}(\mathbf{U}_i^0, \mathbf{U}_j^0) + \frac{\partial \Phi_{ij}}{\partial \mathbf{U}_i} \delta \mathbf{U}_i + \frac{\partial \Phi_{ij}}{\partial \mathbf{U}_j} \delta \mathbf{U}_j. \quad (20)$$

Substituting Equations (19) and (20) into Equation (4), the linear error evolution model is set up

$$\frac{d(\delta \mathbf{U}_i)}{dt} = -\frac{1}{|\Omega_i|} \sum_{\Gamma_{ij} \subset \partial \Omega_i} |\Gamma_{ij}| \left(\frac{\partial \Phi_{ij}}{\partial \mathbf{U}_i} \delta \mathbf{U}_i + \frac{\partial \Phi_{ij}}{\partial \mathbf{U}_j} \delta \mathbf{U}_j \right). \quad (21)$$

The first term on the right-hand side of (21) contains the influence of the error in cell i itself, and the second term contains the influence of the errors in the neighbor cells j . Equation (21) holds for all cells in the computational domain, so we finally get the error evolution of all i cells in the domain

$$\frac{d}{dt} \begin{pmatrix} \delta \mathbf{U}_1 \\ \vdots \\ \delta \mathbf{U}_i \end{pmatrix} = S \begin{pmatrix} \delta \mathbf{U}_1 \\ \vdots \\ \delta \mathbf{U}_i \end{pmatrix}, \quad (22)$$

where S is the stability matrix. When considering only the evolution of initial errors, the solution of the linear time invariant system is

$$\begin{pmatrix} \delta \mathbf{U}_1 \\ \vdots \\ \delta \mathbf{U}_i \end{pmatrix} (t) = \exp^{St} \begin{pmatrix} \delta \mathbf{U}_1 \\ \vdots \\ \delta \mathbf{U}_i \end{pmatrix}_{t=0}, \quad (23)$$

and remains bounded if the maximum of the real part of the eigenvalues of S is nonpositive

$$\max(\operatorname{Re}(\lambda(S))) \leq 0.$$

This linear analysis is carried out on a 2D computational domain $[0, 1] \times [0, 1]$. It is discretized by 11×11 regular Cartesian cells. The numerical setup is set as

$$\mathbf{U}_L = (\rho, u, v, p)_L = \left[1, 1, 0, \frac{1}{\gamma(\gamma-1)M_0^2} + \frac{1}{2} \right], \quad i \leq 5, \quad (24)$$

and

$$\mathbf{U}_R = (\rho, u, v, p)_R = \left[f(M_0), 1, 0, \frac{g(M_0)}{\gamma(\gamma-1)M_0^2} + \frac{1}{2f(M_0)} \right], \quad i \geq 7, \quad (25)$$

with

$$f(M_0) = \left(\frac{2}{(\gamma+1)M_0^2} + \frac{\gamma-1}{\gamma+1} \right)^{-1}, \quad g(M_0) = \frac{2\gamma M_0^2}{\gamma+1} - \frac{\gamma-1}{\gamma+1}, \quad (26)$$

where the upstream Mach number M_0 is set as 7.0. The intermediate shock states ($M: i = 6$) can be calculated following the method presented in the work of Chauvat et al.¹³

The stability of the HLLC-type schemes in the current study has been analyzed. In Figure 2, we present the distribution of the eigenvalues of the stability matrix in the complex plane for different schemes. It can be observed that the

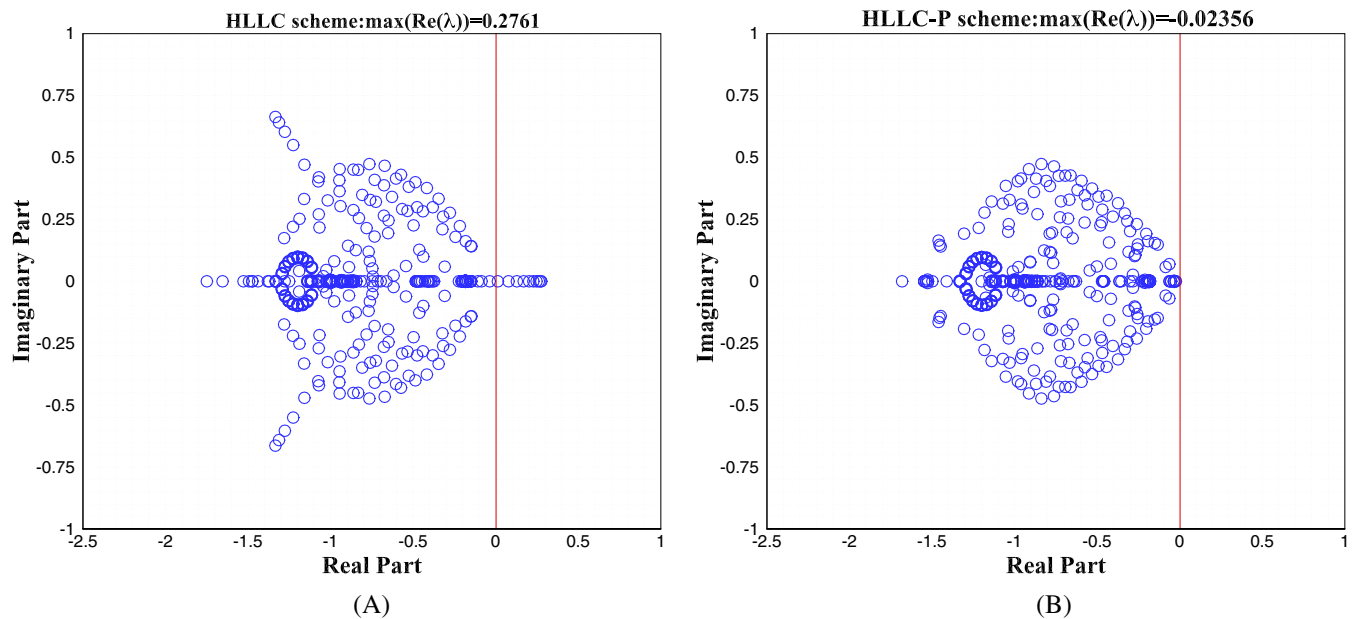


FIGURE 2 The distribution of the eigenvalues of stability matrix in complex plane at $M_0 = 7$ [Colour figure can be viewed at wileyonlinelibrary.com]

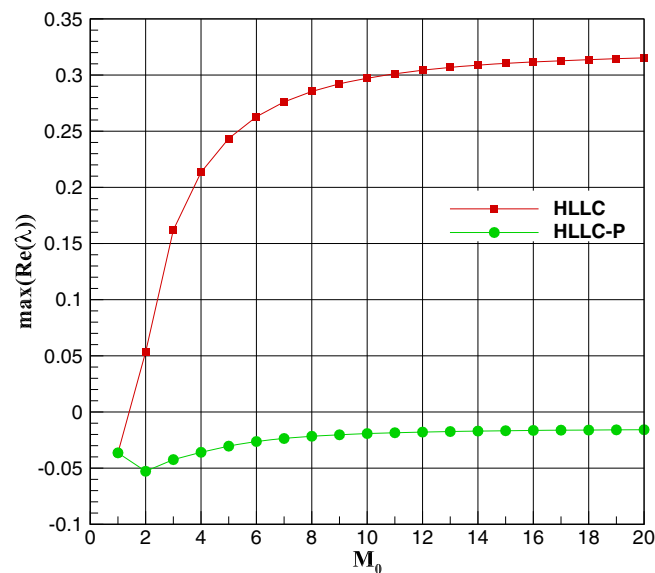


FIGURE 3 The maximal real part of the eigenvalues of stability matrix versus upstream Mach number [Colour figure can be viewed at wileyonlinelibrary.com]

original HLLC scheme has a maximum eigenvalue of 0.2761, which is responsible for its shock instability. With the pressure-control modification, the maximum eigenvalue of the proposed scheme HLLC-P is -0.02356 , demonstrating its stability. In Figure 3, we present the maximal real parts of the eigenvalues of the HLLC-type schemes as functions of the freestream Mach number. It can be observed that the HLLC scheme is always unstable when the upstream Mach number is greater than about 2. However, the HLLC-P scheme is always stable for all Mach numbers. These results show that the pressure-control technique is efficient to suppress the numerical shock instability of the HLLC scheme.

4 | MODIFICATIONS AT LOW MACH NUMBERS

It has been well demonstrated in the work of Volpe²² and Guillard and Viozat²³ that Godunov-type schemes are most of the time not accurate at low Mach number. Dellacherie et al³⁴ theoretically analyze the low Mach number problem in the case of the linear wave equation. It has been pointed out that the profound root of the low Mach number problem is linear. An all Mach correction is proposed and justified in the linear case and then is further extended to the nonlinear compressible Euler system. In this section, we first review the all Mach number correction to Godunov-type schemes proposed by Dellacherie et al³⁴ that solve the compressible Euler system. Then, we apply the all Mach correction to the robust HLLC-type Riemann solver proposed in Equations (15) and (16).

4.1 | Construction of all Mach Godunov-type schemes for the compressible Euler system

The compressible Euler system is solved by a finite volume method with a Godunov-type scheme used to discrete the spatial convective term. Following Dellacherie et al,³⁴ we propose the all Mach Godunov-type scheme

$$\frac{d\mathbf{U}_i}{dt} + \frac{1}{|\Omega_i|} \sum_{\Gamma_{ij} \subset \partial\Omega_i} |\Gamma_{ij}| \Phi_{ij}^{\text{AM},X} = 0, \quad (27)$$

where X denotes a Godunov-type scheme. The numerical flux $\Phi_{ij}^{\text{AM},X}$ can be written in the following expression:

$$\Phi_{ij}^{\text{AM},X} = \Phi_{ij}^X + (1 - \theta_{ij}) \frac{\rho_{ij} c_{ij}}{2} \begin{pmatrix} 0 \\ \Delta q n_x \\ \Delta q n_y \\ 0 \end{pmatrix}, \quad (28)$$

where Φ_{ij}^X is the unmodified flux evaluated by the X scheme, and the weight function θ_{ij} is related to the local Mach number M_{ij}

$$\theta_{ij} = \theta(M_{ij}) \quad \text{with} \quad \theta(M) = \min(M, 1). \quad (29)$$

In Equations (28) and (29), M_{ij} , ρ_{ij} , and c_{ij} are the calculated Mach number, density, and sound speed at the interface. Another expression of the modified numerical flux $\Phi_{ij}^{\text{AM},X}$ can be given by

$$\Phi_{ij}^{\text{AM},X} = \begin{pmatrix} \rho^* q^* \\ \rho^* q^* u^* + p^{**} n_x \\ \rho^* q^* v^* + p^{**} n_y \\ (\rho^* e^* + p^*) q^* \end{pmatrix}_{ij} \quad (30)$$

with

$$p_{ij}^{**} = \theta_{ij} p_{ij}^* + (1 - \theta_{ij}) \frac{p_i + p_j}{2}, \quad (31)$$

where (ρ^*, u^*, v^*, e^*) is solution of a one-dimensional (linearized or nonlinearized) Riemann problem. To complete the evaluation of the scaling function θ_{ij} , one need to determine the definition of the local Mach number M_{ij} . There are many alternatives to the local Mach number, such as those given by Rieper,³⁰ Thornber et al,⁴⁹ and Shima and Kitamura.⁵⁰ Here, we use the following formulation of Mach number

$$M_{ij} = \max \left(\sqrt{u_i^2 + v_i^2} / c_i, \sqrt{u_j^2 + v_j^2} / c_j \right). \quad (32)$$

As argued in the work of Chen et al,⁵¹ this choice of the local Mach number M_{ij} has no effect on the numerical stability near a sonic point or shock wave at high speed flows. What should be noted is that the proposed approach to obtain all Mach schemes is not limited to Godunov-type schemes, it can also be applied to other schemes such as the Rusanov scheme and the Lax-Friedrichs scheme.

4.2 | An all Mach HLLC-type Riemann solver

In this section, we apply the proposed all Mach correction in Equation (30) to cure the accuracy problem of the HLLC-type Riemann solver at low Mach number. Here, the unmodified flux Φ_{ij}^X is the shock-stable HLLC-type scheme defined in

Equation (15) and (16). Following the all Mach correction in (30), the modified numerical fluxes in the star region can be written as

$$\Phi_{\text{AM-HLLC-P,K}}^* = \begin{pmatrix} \rho_K^* S^* \\ \rho_K^* S^* [u_K + n_x (S^* - q_K)] + p^{***} n_x \\ \rho_K^* S^* [v_K + n_y (S^* - q_K)] + p^{***} n_y \\ S^* (\rho_K^* e_K^* + p^*) \end{pmatrix}_{ij} + \Phi_p, \quad (33)$$

where θ_{ij} is defined in Equations (29) and (32), $(\cdot)_{ij}$ are Roe averaged values. According to its original form in (30), the all Mach numerical flux only modifies the pressure term in the star region. It is defined by

$$p^{***} = f p^{**} + (1 - f) p^*, \quad (34)$$

where p^{**} is defined in Equation (31), p^* is defined in Equation (10), f is defined in Equations (17) and (18). As argued in the work of Oßwald et al,³⁷ the all Mach correction term defined in Equation (31) helps to improve the behavior of the scheme at low Mach numbers, but it will introduce small disturbances in the vicinity of shocks. Thus, in the above formulation (34), we apply the pressure weight function in Equations (17) and (18) to turn off the all Mach correction at shocks. In the supersonic regions, the all Mach HLLC-type scheme (ie, AM-HLLC-P) recovers to the original HLLC-P solver.

4.3 | Asymptotic analysis

In order to understand the all Mach correction in (34), we present here an asymptotic analysis. It was first introduced by Guillard and Viozat²³ and followed by many scholars to study asymptotic behaviors of upwind schemes in the incompressible limit. Here, we follow closely the work of Rieper³⁰ and extend the study and strategies therein for the Roe method to the AM-HLLC-P flux. The following nomenclature defined in the work of Rieper³⁰ is used:

i	index vector for cell of reference, $\mathbf{i} = (i, j)$;
$\nu(\mathbf{i})$	index set for neighboring cells, $\nu(\mathbf{i}) = (i \pm 1, j), (i, j \pm 1)$;
l	index vector for neighboring cell, $\mathbf{l} = (i, j \pm 1), (i \pm 1, j)$;
A_i	area of the reference cell;
il	index for edge between cell i and l ;
δ_{il}	length of cell interface il ;
$\mathbf{n}_{il} = (n_x, n_y)_{il}^T$	unit outer normal vector from cell i to l ;
$\Delta_{il} = \phi_i - \phi_l$	difference operator;
ϕ_{il}	Roe average of ϕ_i and ϕ_l ;
$\mathbf{u} = (u, v)^T$	velocity with Cartesian (global) coordinates;
$q = \mathbf{u} \cdot \mathbf{n}$	normal component of \mathbf{u} .

For simplicity, we consider a uniform Cartesian grid with $\delta_{ij} = \Delta x = \Delta y = \delta$ and $A_i = \Delta x \Delta y = \delta^2$. Substituting the AM-HLLC-P flux into Equation (4), one can obtain the semidiscrete equations which are recalled in Appendix A.

As in the continuous asymptotic analysis, we assume for all physical quantities ϕ an asymptotic three-term expansion

$$\phi = \phi^{(0)} + M \phi^{(1)} + M^2 \phi^{(2)} + O(M^2) \quad \text{as } M \rightarrow 0 \quad (35)$$

and insert these expansions in the discrete equations. They read, sorted by powers of the Mach number:

Order M^{-1} :

$$\sum_{l \in \nu(\mathbf{i})} \left\{ \frac{1}{2} p_1^{(0)} (n_x)_{il} + \frac{(n_x)_{il} \rho_i^{(0)} a_i^{(0)} (\Delta_{il} p^{(0)})^2}{\left(\rho_i^{(0)} a_i^{(0)} + \rho_l^{(0)} a_l^{(0)} \right) \Delta_{il} p^{(0)} + \left(\rho_i^{(0)} a_i^{(0)} + \rho_l^{(0)} a_l^{(0)} \right)^2 a_i^{(0)}} \right\} \delta_{il} = 0, \quad (36)$$

$$\sum_{l \in \nu(\mathbf{i})} \left\{ \frac{1}{2} p_1^{(0)} (n_y)_{il} + \frac{(n_y)_{il} \rho_i^{(0)} a_i^{(0)} (\Delta_{il} p^{(0)})^2}{\left(\rho_i^{(0)} a_i^{(0)} + \rho_l^{(0)} a_l^{(0)} \right) \Delta_{il} p^{(0)} + \left(\rho_i^{(0)} a_i^{(0)} + \rho_l^{(0)} a_l^{(0)} \right)^2 a_i^{(0)}} \right\} \delta_{il} = 0. \quad (37)$$

Order M^0 :

$$\sum_{l \in \nu(\mathbf{i})} \frac{\rho_i^{(0)} a_i^{(0)} \Delta_{il} p^{(0)}}{\Delta_{il} p^{(0)} + \left(\rho_i^{(0)} a_i^{(0)} + \rho_l^{(0)} a_l^{(0)} \right) a_i^{(0)}} \delta_{il} = 0, \quad (38)$$

Order M^1 :

$$A_i \frac{d}{dt} \rho_i^{(0)} + \sum_{I \in v(i)} \left\{ \frac{(\rho_i a_i \Delta_{II} p)^{(1)} + \rho_i^{(0)} a_i^{(0)} (\rho_i^{(0)} a_i^{(0)} q_i^{(0)} + \rho_1^{(0)} a_1^{(0)} q_1^{(0)})}{\Delta_{II} p^{(0)} + (\rho_i^{(0)} a_i^{(0)} + \rho_1^{(0)} a_1^{(0)}) a_i^{(0)}} \right. \\ \left. - \frac{\rho_i^{(0)} a_i^{(0)} (\Delta_{II} p + \rho_i a_i^2 + \rho_1 a_1 a_i)^{(1)} \Delta_{II} p^{(0)} - \rho_i^{(0)} a_i^{(0)} \rho_1^{(0)} a_1^{(0)} \Delta_{II} p^{(0)} \Delta_{II} q^{(0)}}{[\Delta_{II} p^{(0)} + (\rho_i^{(0)} a_i^{(0)} + \rho_1^{(0)} a_1^{(0)}) a_i^{(0)}]^2} \right\} \delta_{II} = 0, \quad (42)$$

$$A_i \frac{d}{dt} (\rho_i u_i)^{(0)} + \sum_{I \in v(i)} \left\{ \frac{[\rho_i a_i (n_x)_{II} (\Delta_{II} p)^2]^{(2)} + \{\rho_i a_i \Delta_{II} p \{ \rho_i a_i (u_i + (n_x)_{II} q_i) + \rho_1 a_1 [u_i - (n_x)_{II} (\Delta_{II} q - q_1)] \}\}^{(1)}}{\Delta_{II} p^{(0)} (\rho_i^{(0)} a_i^{(0)} + \rho_1^{(0)} a_1^{(0)}) + a_i^{(0)} (\rho_i^{(0)} a_i^{(0)} + \rho_1^{(0)} a_1^{(0)})^2} \right. \\ + \frac{\rho_i^{(0)} a_i^{(0)} (\rho_i^{(0)} a_i^{(0)} q_i^{(0)} + \rho_1^{(0)} a_1^{(0)} q_1^{(0)}) [\rho_i^{(0)} a_i^{(0)} u_i^{(0)} + \rho_1^{(0)} a_1^{(0)} (u_i^{(0)} - (n_x)_{II} \Delta_{II} q^{(0)})]}{\Delta_{II} p^{(0)} (\rho_i^{(0)} a_i^{(0)} + \rho_1^{(0)} a_1^{(0)}) + a_i^{(0)} (\rho_i^{(0)} a_i^{(0)} + \rho_1^{(0)} a_1^{(0)})^2} \\ - \frac{\rho_i^{(0)} a_i^{(0)} (\Delta_{II} p^{(0)})^2 (n_x)_{II} \{ [\Delta_{II} p (\rho_i a_i + \rho_1 a_1) + a_i (\rho_i a_i + \rho_1 a_1)^2]^{(2)} - [\rho_1 a_1 (\rho_i a_i + \rho_1 a_1) \Delta_{II} q]^{(1)} \}}{[\Delta_{II} p^{(0)} (\rho_i^{(0)} a_i^{(0)} + \rho_1^{(0)} a_1^{(0)}) + a_i^{(0)} (\rho_i^{(0)} a_i^{(0)} + \rho_1^{(0)} a_1^{(0)})^2]^2} \\ - \frac{[\rho_i a_i (n_x)_{II} (\Delta_{II} p)^2]^{(1)} + \rho_i^{(0)} a_i^{(0)} \Delta_{II} p^{(0)} \{ \rho_i^{(0)} a_i^{(0)} (u_i^{(0)} + (n_x)_{II} q_i^{(0)}) + \rho_1^{(0)} a_1^{(0)} [u_i^{(0)} - (n_x)_{II} (\Delta_{II} q^{(0)} - q_1^{(0)})] \}}{[\Delta_{II} p^{(0)} (\rho_i^{(0)} a_i^{(0)} + \rho_1^{(0)} a_1^{(0)}) + a_i^{(0)} (\rho_i^{(0)} a_i^{(0)} + \rho_1^{(0)} a_1^{(0)})^2]^2} \\ - \frac{\{ [\Delta_{II} p (\rho_i a_i + \rho_1 a_1) + a_i (\rho_i a_i + \rho_1 a_1)^2]^{(1)} - \rho_1^{(0)} a_1^{(0)} (\rho_i^{(0)} a_i^{(0)} + \rho_1^{(0)} a_1^{(0)}) \Delta_{II} q^{(0)} \}}{[\Delta_{II} p^{(0)} (\rho_i^{(0)} a_i^{(0)} + \rho_1^{(0)} a_1^{(0)}) + a_i^{(0)} (\rho_i^{(0)} a_i^{(0)} + \rho_1^{(0)} a_1^{(0)})^2]^2} \\ + \frac{\rho_i^{(0)} a_i^{(0)} (n_x)_{II} (\Delta_{II} p^{(0)})^2 \{ [\Delta_{II} p (\rho_i a_i + \rho_1 a_1) + a_i (\rho_i a_i + \rho_1 a_1)^2]^{(1)} - \rho_1^{(0)} a_1^{(0)} (\rho_i^{(0)} a_i^{(0)} + \rho_1^{(0)} a_1^{(0)}) \Delta_{II} q^{(0)} \}}{[\Delta_{II} p^{(0)} (\rho_i^{(0)} a_i^{(0)} + \rho_1^{(0)} a_1^{(0)}) + a_i^{(0)} (\rho_i^{(0)} a_i^{(0)} + \rho_1^{(0)} a_1^{(0)})^2]^3} \\ + \frac{\frac{1}{2} \{ (\rho_i a_i + \rho_1 a_1) [p_i + p_1 - \theta_{II} \cdot \Delta_{II} p] \}^{(2)} + (\theta_{II} \rho_i a_i \rho_1 a_1 \Delta_{II} q)^{(1)}}{\rho_i^{(0)} a_i^{(0)} + \rho_1^{(0)} a_1^{(0)}} (n_x)_{II} \\ - \frac{\frac{1}{2} [p_i^{(0)} + p_1^{(0)} - \theta_{II} \cdot \Delta_{II} p^{(0)}] \cdot (\rho_i a_i + \rho_1 a_1)^{(2)}}{\rho_i^{(0)} a_i^{(0)} + \rho_1^{(0)} a_1^{(0)}} (n_x)_{II} \\ - \frac{\{ \frac{1}{2} \{ (\rho_i a_i + \rho_1 a_1) (p_i + p_1 - \theta \cdot \Delta_{II} p) \}^{(1)} + \theta_{II} \rho_i^{(0)} a_i^{(0)} \rho_1^{(0)} a_1^{(0)} \Delta_{II} q^{(0)} \} \cdot (\rho_i a_i + \rho_1 a_1)^{(1)}}{(\rho_i^{(0)} a_i^{(0)} + \rho_1^{(0)} a_1^{(0)})^2} (n_x)_{II} \\ + \frac{\frac{1}{2} (p_i^{(0)} + p_1^{(0)} - \theta_{II} \cdot \Delta_{II} p^{(0)}) \cdot [(\rho_i a_i + \rho_1 a_1)^{(1)}]^2}{(\rho_i^{(0)} a_i^{(0)} + \rho_1^{(0)} a_1^{(0)})^2} (n_x)_{II} \left. \right\} \delta_{II} = 0, \quad (43)$$

$$\begin{aligned}
& A_i \frac{d}{dt} (\rho_i v_i)^{(0)} + \sum_{\mathbf{l} \in \mathbf{v}(\mathbf{i})} \left\{ \frac{\left[\rho_i a_i (n_y)_{\mathbf{il}} (\Delta_{\mathbf{il}} p)^2 \right]^{(2)} + \left\{ \rho_i a_i \Delta_{\mathbf{il}} p \left\{ \rho_i a_i (u_i + (n_y)_{\mathbf{il}} q_i) + \rho_l a_l [v_i - (n_y)_{\mathbf{il}} (\Delta_{\mathbf{il}} q - q_l)] \right\} \right\}^{(1)}}{\Delta_{\mathbf{il}} p^{(0)} \left(\rho_i^{(0)} a_i^{(0)} + \rho_l^{(0)} a_l^{(0)} \right) + a_i^{(0)} \left(\rho_i^{(0)} a_i^{(0)} + \rho_l^{(0)} a_l^{(0)} \right)^2} \right. \\
& + \frac{\rho_i^{(0)} a_i^{(0)} \left(\rho_i^{(0)} a_i^{(0)} q_i^{(0)} + \rho_l^{(0)} a_l^{(0)} q_l^{(0)} \right) \left[\rho_i^{(0)} a_i^{(0)} v_i^{(0)} + \rho_l^{(0)} a_l^{(0)} \left(v_i^{(0)} - (n_y)_{\mathbf{il}} \Delta_{\mathbf{il}} q^{(0)} \right) \right]}{\Delta_{\mathbf{il}} p^{(0)} \left(\rho_i^{(0)} a_i^{(0)} + \rho_l^{(0)} a_l^{(0)} \right) + a_i^{(0)} \left(\rho_i^{(0)} a_i^{(0)} + \rho_l^{(0)} a_l^{(0)} \right)^2} \\
& - \frac{\rho_i^{(0)} a_i^{(0)} (\Delta_{\mathbf{il}} p^{(0)})^2 (n_y)_{\mathbf{il}} \left\{ \left[\Delta_{\mathbf{il}} p (\rho_i a_i + \rho_l a_l) + a_i (\rho_i a_i + \rho_l a_l)^2 \right]^{(2)} - \left[\rho_l a_l (\rho_i a_i + \rho_l a_l) \Delta_{\mathbf{il}} q \right]^{(1)} \right\}}{\left[\Delta_{\mathbf{il}} p^{(0)} \left(\rho_i^{(0)} a_i^{(0)} + \rho_l^{(0)} a_l^{(0)} \right) + a_i^{(0)} \left(\rho_i^{(0)} a_i^{(0)} + \rho_l^{(0)} a_l^{(0)} \right)^2 \right]^2} \\
& - \frac{\left[\rho_i a_i (n_y)_{\mathbf{il}} (\Delta_{\mathbf{il}} p)^2 \right]^{(1)} + \rho_i^{(0)} a_i^{(0)} \Delta_{\mathbf{il}} p^{(0)} \left\{ \rho_i^{(0)} a_i^{(0)} \left(v_i^{(0)} + (n_y)_{\mathbf{il}} q_i^{(0)} \right) + \rho_l^{(0)} a_l^{(0)} \left[v_i^{(0)} - (n_y)_{\mathbf{il}} (\Delta_{\mathbf{il}} q^{(0)} - q_l^{(0)}) \right] \right\}}{\left[\Delta_{\mathbf{il}} p^{(0)} \left(\rho_i^{(0)} a_i^{(0)} + \rho_l^{(0)} a_l^{(0)} \right) + a_i^{(0)} \left(\rho_i^{(0)} a_i^{(0)} + \rho_l^{(0)} a_l^{(0)} \right)^2 \right]^2} \\
& \cdot \frac{\left\{ \left[\Delta_{\mathbf{il}} p (\rho_i a_i + \rho_l a_l) + a_i (\rho_i a_i + \rho_l a_l)^2 \right]^{(1)} - \rho_l^{(0)} a_l^{(0)} \left(\rho_i^{(0)} a_i^{(0)} + \rho_l^{(0)} a_l^{(0)} \right) \Delta_{\mathbf{il}} q^{(0)} \right\}}{\left[\Delta_{\mathbf{il}} p^{(0)} \left(\rho_i^{(0)} a_i^{(0)} + \rho_l^{(0)} a_l^{(0)} \right) + a_i^{(0)} \left(\rho_i^{(0)} a_i^{(0)} + \rho_l^{(0)} a_l^{(0)} \right)^2 \right]^2} \\
& + \frac{\rho_i^{(0)} a_i^{(0)} (n_y)_{\mathbf{il}} (\Delta_{\mathbf{il}} p^{(0)})^2 \left\{ \left[\Delta_{\mathbf{il}} p (\rho_i a_i + \rho_l a_l) + a_i (\rho_i a_i + \rho_l a_l)^2 \right]^{(1)} - \rho_l^{(0)} a_l^{(0)} \left(\rho_i^{(0)} a_i^{(0)} + \rho_l^{(0)} a_l^{(0)} \right) \Delta_{\mathbf{il}} q^{(0)} \right\}^2}{\left[\Delta_{\mathbf{il}} p^{(0)} \left(\rho_i^{(0)} a_i^{(0)} + \rho_l^{(0)} a_l^{(0)} \right) + a_i^{(0)} \left(\rho_i^{(0)} a_i^{(0)} + \rho_l^{(0)} a_l^{(0)} \right)^2 \right]^3} \\
& + \frac{\frac{1}{2} \left\{ (\rho_i a_i + \rho_l a_l) [p_i + p_l - \theta_{\mathbf{il}} \cdot \Delta_{\mathbf{il}} p] \right\}^{(2)} + (\theta_{\mathbf{il}} \rho_i a_i \rho_l a_l \Delta_{\mathbf{il}} q)^{(1)}}{\rho_i^{(0)} a_i^{(0)} + \rho_l^{(0)} a_l^{(0)}} (n_y)_{\mathbf{il}} \\
& - \frac{\frac{1}{2} \left[p_i^{(0)} + p_l^{(0)} - \theta_{\mathbf{il}} \cdot \Delta_{\mathbf{il}} p^{(0)} \right] \cdot (\rho_i a_i + \rho_l a_l)^{(2)}}{\rho_i^{(0)} a_i^{(0)} + \rho_l^{(0)} a_l^{(0)}} (n_y)_{\mathbf{il}} \\
& - \frac{\left\{ \frac{1}{2} \{ (\rho_i a_i + \rho_l a_l) (p_i + p_l - \theta \cdot \Delta_{\mathbf{il}} p) \}^{(1)} + \theta_{\mathbf{il}} \rho_i^{(0)} a_i^{(0)} \rho_l^{(0)} a_l^{(0)} \Delta_{\mathbf{il}} q^{(0)} \right\} \cdot (\rho_i a_i + \rho_l a_l)^{(1)}}{\left(\rho_i^{(0)} a_i^{(0)} + \rho_l^{(0)} a_l^{(0)} \right)^2} (n_y)_{\mathbf{il}} \\
& + \frac{\frac{1}{2} \left(p_i^{(0)} + p_l^{(0)} - \theta_{\mathbf{il}} \cdot \Delta_{\mathbf{il}} p^{(0)} \right) \cdot \left[(\rho_i a_i + \rho_l a_l)^{(1)} \right]^2}{\left(\rho_i^{(0)} a_i^{(0)} + \rho_l^{(0)} a_l^{(0)} \right)^2} (n_y)_{\mathbf{il}} \left. \right\} \delta_{\mathbf{il}} = 0, \tag{44}
\end{aligned}$$

$$\begin{aligned}
A_i \frac{d}{dt} (\rho_i e_i)^{(0)} + \sum_{l \in v(i)} \left\{ \frac{[\rho_i a_i h_i (\rho_i a_i + \rho_l a_l) \Delta_{il} p - \rho_i a_i^2 (\Delta_{il} p)^2]^{(1)} + \rho_i^{(0)} a_i^{(0)} q_i^{(0)} (\Delta_{il} p^{(0)})^2}{(\rho_i^{(0)} a_i^{(0)} + \rho_l^{(0)} a_l^{(0)}) [\Delta_{il} p^{(0)} + a_i^{(0)} (\rho_i^{(0)} a_i^{(0)} + \rho_l^{(0)} a_l^{(0)})]} \right. \\
+ \frac{[\rho_i^{(0)} (a_i^{(0)})^2 \rho_l^{(0)} a_l^{(0)} (\Delta_{il} q^{(0)} - q_l^{(0)}) - (\rho_i^{(0)})^2 (a_i^{(0)})^3 q_i^{(0)}] \Delta_{il} p^{(0)}}{(\rho_i^{(0)} a_i^{(0)} + \rho_l^{(0)} a_l^{(0)}) [\Delta_{il} p^{(0)} + a_i^{(0)} (\rho_i^{(0)} a_i^{(0)} + \rho_l^{(0)} a_l^{(0)})]} \\
+ \frac{\rho_i^{(0)} a_i^{(0)} h_i^{(0)} (\rho_i^{(0)} a_i^{(0)} q_i^{(0)} + \rho_l^{(0)} a_l^{(0)} q_l^{(0)})}{\Delta_{il} p^{(0)} + a_i^{(0)} (\rho_i^{(0)} a_i^{(0)} + \rho_l^{(0)} a_l^{(0)})} \\
- \rho_i^{(0)} a_i^{(0)} \Delta_{il} p^{(0)} h_i^{(0)} \frac{[(\rho_i a_i + \rho_l a_l) \Delta_{il} p + a_i (\rho_i a_i + \rho_l a_l)^2]^{(1)}}{(\rho_i^{(0)} a_i^{(0)} + \rho_l^{(0)} a_l^{(0)}) [\Delta_{il} p^{(0)} + a_i^{(0)} (\rho_i^{(0)} a_i^{(0)} + \rho_l^{(0)} a_l^{(0)})]^2} \\
+ \rho_i^{(0)} (a_i^{(0)} \Delta_{il} p^{(0)})^2 \frac{[(\rho_i a_i + \rho_l a_l) \Delta_{il} p + a_i (\rho_i a_i + \rho_l a_l)^2]^{(1)}}{(\rho_i^{(0)} a_i^{(0)} + \rho_l^{(0)} a_l^{(0)})^2 [\Delta_{il} p^{(0)} + a_i^{(0)} (\rho_i^{(0)} a_i^{(0)} + \rho_l^{(0)} a_l^{(0)})]^2} \\
+ \rho_i^{(0)} a_i^{(0)} \Delta_{il} p^{(0)} h_i^{(0)} \frac{\rho_l^{(0)} a_l^{(0)} \Delta_{il} q^{(0)}}{[\Delta_{il} p^{(0)} + a_i^{(0)} (\rho_i^{(0)} a_i^{(0)} + \rho_l^{(0)} a_l^{(0)})]^2} \\
\left. - \rho_i^{(0)} (a_i^{(0)} \Delta_{il} p^{(0)})^2 \frac{\rho_l^{(0)} a_l^{(0)} \Delta_{il} q^{(0)}}{(\rho_i^{(0)} a_i^{(0)} + \rho_l^{(0)} a_l^{(0)}) [\Delta_{il} p^{(0)} + a_i^{(0)} (\rho_i^{(0)} a_i^{(0)} + \rho_l^{(0)} a_l^{(0)})]^2} \right\} \delta_{il} = 0. \quad (45)
\end{aligned}$$

Pressure fluctuations of order M^2 :

Similar to the study in the work of Guillard and Viozat,²³ Equations (36), (37) and (38) or (41) imply the uniformity of the leading order pressure in space

$$p_i^{(0)} = \text{const} \quad \text{for all } i. \quad (46)$$

The evolution equation for $p^{(0)}$ can be obtained by replacing the energy density $(\rho e)^{(0)}$ in Equation (45) by the pressure $p^{(0)}$

$$(\rho_i e_i)^{(0)} = \frac{1}{\gamma - 1} p_i^{(0)}. \quad (47)$$

This formulation is a result of an asymptotic analysis of the thermodynamic relations, (readers are referred to the work of Rieper³⁰ for the detail derivation). Considering the fact $\Delta_{il} p^{(0)} = 0$ and replacing the Roe averages of constant quantities by their constant values $\rho_{il}^{(0)} = \rho^{(0)}$ and $a_{il}^{(0)} = a^{(0)}$, Equation (45) can be simplified into the following form:

$$\frac{d}{dt} p^{(0)} + \gamma p^{(0)} \frac{1}{A_i} \sum_{l \in v(i)} \frac{\mathbf{u}_l^{(0)} \cdot \mathbf{n}_{il}}{2} \delta_{il} = -\frac{1}{2} a^{(0)} \frac{1}{A_i} \sum_{l \in v(i)} \Delta_{il} p^{(1)} \delta_{il}. \quad (48)$$

Under the assumption that there is no net influx over the boundary due to $u^{(0)}$ in the ghost cells and there is no gradient in $p^{(0)}$ across the boundary, the above equation can be further simplified into

$$\gamma p^{(0)} \frac{1}{A_i} \sum_{l \in v(i)} \frac{\mathbf{u}_l^{(0)} \cdot \mathbf{n}_{il}}{2} \delta_{il} = -\frac{1}{2} a^{(0)} \frac{1}{A_i} \sum_{l \in v(i)} \Delta_{il} p^{(1)} \delta_{il} \quad (49)$$

with $p^{(0)} = \text{constant}$.

	A	C	A	C
	B	D	B	D
	A	C	A	C
	B	D	B	D

FIGURE 4 Four-field solution

Similarly, the spatial relation for the first-order pressure $p^{(1)}$ can also be derived from Equations (39) and (40). In these equations, the terms in brackets with a superscript can be expanded using the rules for asymptotic expressions, we obtain

$$\begin{aligned} \sum_{\mathbf{l} \in \mathbf{v}(\mathbf{i})} p_1^{(1)}(n_x)_{\mathbf{il}} \delta_{\mathbf{il}} &= 0, \\ \sum_{\mathbf{l} \in \mathbf{v}(\mathbf{i})} p_1^{(1)}(n_y)_{\mathbf{il}} \delta_{\mathbf{il}} &= 0. \end{aligned} \quad (50)$$

One can infer from Equations (50) that the first-order pressure satisfies the following relation:

$$\begin{aligned} p_{i+1,j}^{(1)} - p_{i-1,j}^{(1)} &= 0, \\ p_{i,j+1}^{(1)} - p_{i,j-1}^{(1)} &= 0. \end{aligned} \quad (51)$$

This would still allow a four-field checkerboard structure in the flow domain as depicted in Figure 4. However, such checkerboard modes will be damped away by the numerical viscosity due to the maintained upwinding in the momentum equations. To this end, we need to derive the evolution for the divergence of $\mathbf{u}^{(0)}$. Assuming that the leading-order density and the leading-order speed of sound are constant, and considering the fact in Equation (51), the momentum Equations (36) and (37) can be transformed into the following form:

$$\begin{aligned} \rho_i^{(0)} A_i \frac{d}{dt} \mathbf{u}_i^{(0)} + \sum_{\mathbf{l} \in \mathbf{v}(\mathbf{i})} \left\{ \frac{p_1^{(2)}}{2} \mathbf{n}_{\mathbf{il}} + \frac{\Delta_{\mathbf{il}} p^{(1)} (\mathbf{u}_i^{(0)} + q_1^{(0)} \mathbf{n}_{\mathbf{il}})}{2a^{(0)}} + \frac{1}{2} \rho^{(0)} \mathbf{u}_i^{(0)} q_1^{(0)} \right. \\ \left. + \frac{\theta_{\mathbf{il}} \rho^{(0)} a^{(0)} \Delta_{\mathbf{il}} q^{(0)}}{2} \mathbf{n}_{\mathbf{il}} - \frac{\theta_{\mathbf{il}} (\rho_i a_i + \rho_l a_l)^{(1)} \Delta_{\mathbf{il}} q^{(0)}}{4} \mathbf{n}_{\mathbf{il}} \right\} \delta_{\mathbf{il}} = 0. \end{aligned} \quad (52)$$

The time change of the divergence can be obtained by differencing the above momentum equations using the following definition:

$$D_i \mathbf{u}^{(0)} := \frac{u_{i+1,j}^{(0)} - u_{i-1,j}^{(0)} + v_{i,j+1}^{(0)} - v_{i,j-1}^{(0)}}{\delta}. \quad (53)$$

The resulting evolution for the divergence of $\mathbf{u}^{(0)}$ can be written by

$$\frac{d}{dt} D \mathbf{u}^{(0)} = T(D \mathbf{u}^{(0)}) + L p^{(2)} + L(D \mathbf{u}^{(0)}) \delta + R \delta^2. \quad (54)$$

Similar to the argument in the work of Rieper,³⁰ we can observe from Equation (54) that the first term on the RHS describes the transport of the divergence and the second is the Laplacian of $p^{(2)}$. The third denotes a numerical damping of the divergence, which is the term that works. It shows that the unphysical divergence field in $\mathbf{u}^{(0)}$ will damped away in time. The fourth is a rest term.

It follows from Equation (54) that $D \mathbf{u}^{(0)} = 0$ in the limit for large times. Considering this fact and Equation (49), we will obtain that $L p^{(1)} = 0$. This implies the equality of all checkerboard values, ie, $A = B = C = D$, and thus, the checkerboard will vanish in the limit for large times. Thus, the uniformity of $p^{(1)}$ is satisfied on the discrete level, ie, $p^{(1)} = \text{constant}$. Therefore, the discrete solution of the AM-HLLC-P scheme supports pressure fluctuations of order M^2

$$p(\mathbf{x}, t) = p^{(0)}(t) + M^2 p^{(2)}(\mathbf{x}, t). \quad (55)$$

Divergence constraint:

Consider the fact $\Delta_{\text{II}} p^{(1)} = 0$, then Equation (49) becomes

$$\gamma p^{(0)} \frac{1}{A_i} \sum_{\text{I} \in \text{v}(\text{i})} \frac{\mathbf{u}_i^{(0)} \cdot \mathbf{n}_{\text{II}}}{2} \delta_{\text{II}} = 0; \quad (56)$$

thus, the divergence constraint is satisfied on the discrete level, ie

$$\gamma p^{(0)} \tilde{\nabla} \cdot \mathbf{u}^{(0)} = 0, \quad (57)$$

where $\tilde{\nabla} \cdot$ symbolizes the discrete divergence operator.

Poisson equation:

For the current method, we have shown that the divergence constraint is satisfied and the first-order pressure is uniform in the computational field, ie, $\Delta_{\text{II}} p^{(1)} = 0$. Considering these facts, Equation (52) implies a Poisson equation of the following form:

$$\tilde{\nabla}^2 p^{(2)} = f(\mathbf{x}, \mathbf{u}^{(0)}, \rho^{(0)}), \quad (58)$$

where $\tilde{\nabla}^2$ symbolizes the discrete Laplacian operator.

5 | PROPERTIES OF THE NUMERICAL FLUX

In this section, we make efforts to clarify whether the modified terms introduced by the pressure-control technique and the all Mach correction method will influence the desirable properties of the original HLLC scheme. Here, we follow closely the work of Batten et al⁵² and extend the study and strategies therein for the HLLC method to the AM-HLLC-P flux.

5.1 | Exact resolution of isolated contacts

At an isolated contact surface or slip line, there is

$$q = q_L = q_R, \quad p = p_L = p_R. \quad (59)$$

Substituting (59) into (33) and (34), one can observe that the modified pressure-control term Φ_p vanishes. The wave speed S^* defined in Equation (10) can be further simplified into

$$S^* = q, \quad (60)$$

and the modified pressure p^{***} can be simplified into

$$p^{***} = p^* = p. \quad (61)$$

Thus, the corresponding exact solution for a general x/t can be obtained from (5), that is,

$$\mathbf{U}^* = \begin{cases} \mathbf{U}_L, & \text{if } x/t < q, \\ \mathbf{U}_R, & \text{if } x/t > q. \end{cases} \quad (62)$$

5.2 | Exact resolution of isolated shocks

In the situation where an isolated shock wave exists, the exact solution for a general x/t is given by

$$\mathbf{U} = \begin{cases} \mathbf{U}_L, & \text{if } x/t < s, \\ \mathbf{U}_R, & \text{if } x/t > s, \end{cases} \quad (63)$$

where s represents the shock velocity, it is given by the largest (or smallest) eigenvalue of the Roe matrix.² In this case, the pressure dissipative term defined in Equation (16) vanishes and the modified pressure p^{***} in the star region approaches its original form p^* . In this case, the AM-HLLC-P recovers to the HLLC flux. As shown in the work of Batten et al,⁵² the HLLC scheme with the wave speed estimate (14) is able to preserve isolated shocks exactly. Thus, the AM-HLLC-P preserves the property of resolving isolated shocks exactly of the original HLLC scheme.

5.3 | Positivity preservation

As argued by Einfeldt et al,⁴⁴ a Riemann solver yields a positively conservative scheme if all the states generated are physically real. This set of physically realistic states is defined as follows:

$$\mathbf{G} = \left\{ \begin{bmatrix} \rho \\ \rho u \\ \rho v \\ \rho e \end{bmatrix}, \rho > 0, e - \frac{1}{2}(u^2 + v^2) > 0 \right\}, \quad (64)$$

when $\mathbf{U}_L \in \mathbf{G}, \mathbf{U}_R \in \mathbf{G}$, we require that all intermediate states $\mathbf{U}_L^*, \mathbf{U}_R^*$, satisfy the above positive condition, that is,

$$\rho_K^* > 0, \quad (65)$$

$$e_K^* - \frac{1}{2}(u_K^{*2} + v_K^{*2}) > 0. \quad (66)$$

At any rarefaction, the wave speed estimate yields

$$S_L < q_L, \quad S_R > q_R, \quad \text{and} \quad S_L < S^* < S_R. \quad (67)$$

From Equation (9) and (11), one can obtain

$$\rho_K^* = \frac{\rho_K (S_K - q_K)}{S_K - S^*} > 0. \quad (68)$$

In addition, from (9) and (11), the following states can be given by:

$$\begin{aligned} e_K^* &= e_K + (S^* - q_K) \left[S^* + \frac{p_K}{\rho_K (S_K - q_K)} \right], \\ u_K^* &= u_K + n_x (S^* - q_K), \\ v_K^* &= v_K + n_y (S^* - q_K). \end{aligned} \quad (69)$$

Substituting Equation (9) into (66), inequality (66) becomes

$$\begin{aligned} e_K^* - \frac{1}{2}(u_K^{*2} + v_K^{*2}) &= e_K + (S^* - q_K) \left[S^* + \frac{p_K}{\rho_K (S_K - q_K)} \right] \\ &\quad - \frac{1}{2} [u_K + n_x (S^* - q_K)]^2 - \frac{1}{2} [v_K + n_y (S^* - q_K)]^2 \\ &= \frac{1}{2} (S^* - q_K)^2 + \frac{p_K}{\rho_K (S_K - q_K)} (S^* - q_K) + \frac{p_K}{\rho_K (\gamma - 1)} > 0. \end{aligned} \quad (70)$$

The sufficient condition to keep $e_K^* - \frac{1}{2}(u_K^{*2} + v_K^{*2}) > 0$ is to let the discriminant of the above quadratic with respect to $(S^* - q_K)$ be negative

$$\Delta = \left[\frac{p_K}{\rho_K (S_K - q_K)} \right]^2 - 2 \frac{p_K}{\rho_K (\gamma - 1)} < 0. \quad (71)$$

This gives the condition

$$S_K < q_K - \sqrt{\frac{\gamma - 1}{2\gamma}} c_K, \quad (72)$$

and this condition is always satisfied by the wave speed estimates defined in (13) or (14).

5.4 | Efficiency

In Table 1, we present a cost comparison of the HLLC-type schemes. Due to the additional terms introduced by the pressure-control technique and the all Mach correction method, the AM-HLLC-P flux is more expensive. We calculate an average CPU time per time step for different fluxes. As shown in Table 1, the new flux function requires only 18% more CPU time than the original HLLC flux.

TABLE 1 Comparison of computational time

Scheme	HLLC	AM-HLLC-P
Time/time _{HLLC}	1.0	1.18

6 | NUMERICAL EXPERIMENTS

In this section, we will present numerical results of the proposed method for flows with Mach numbers ranging from 0.001 to 20. The flow regimes of the numerical tests cover from low Mach number incompressible flows to hypersonic compressible flows. The results computed by the proposed method are compared with those of other Riemann solvers to show the improvements.

6.1 | A modified Sod's shock tube problem

In the first test case, we consider whether the proposed HLLC-type scheme satisfies the entropy condition. This test is a modified version of the popular Sod's shock tube problem.⁵³ The solution consists of a right shock wave, a right traveling contact wave and a left sonic rarefaction wave.⁴² The initial conditions are given by

$$(\rho_L, u_L, p_L) = (1.0, 0.75, 1.0), \quad \text{and} \quad (\rho_R, u_R, p_R) = (0.125, 0.0, 0.1),$$

where the discontinuity is set at the position $x = 0.3$. The grid is taken as a uniform mesh of 400 cells in the interval $0 < x < 1$. The time step is determined from the local CFL condition with $\text{CFL} = 0.9$, nonreflecting boundary conditions are used at the boundaries. In Figure 5, first-order solutions computed with the HLLC and AM-HLLC-P schemes at time $t = 0.2$ seconds are shown, and the exact solution is also included for comparison. As shown, the results for the AM-HLLC-P scheme are almost the same as that of the HLLC scheme, the sonic rarefaction is resolved well by both methods, and they all show a correct agreement with the exact solution.

6.2 | Double rarefaction problem

In our second test case, we consider whether the proposed HLLC-type scheme is positively conservative. The test case used here is the double rarefaction problem whose solution consists of two rarefaction waves and a trivial contact wave of zero speed. The region between the two nonlinear waves is close to vacuum, which makes this problem a suitable test for assessing the performance of numerical methods for low-density flows.⁴² The initial conditions are given by

$$(\rho_L, u_L, p_L) = (1.0, -2.0, 0.4), \quad \text{and} \quad (\rho_R, u_R, p_R) = (1.0, 2.0, 0.4),$$

where the discontinuity is set at the position $x = 0.5$. The spatial domain is the interval $[0, 1]$, which is discretized with 400 uniform cells. The Courant number coefficient is set as $\text{CFL} = 0.9$, boundary conditions are transmissive. In Figure 6, we compare the first-order solutions for HLLC-type schemes with the exact solution at time $t = 0.15$ seconds. The results

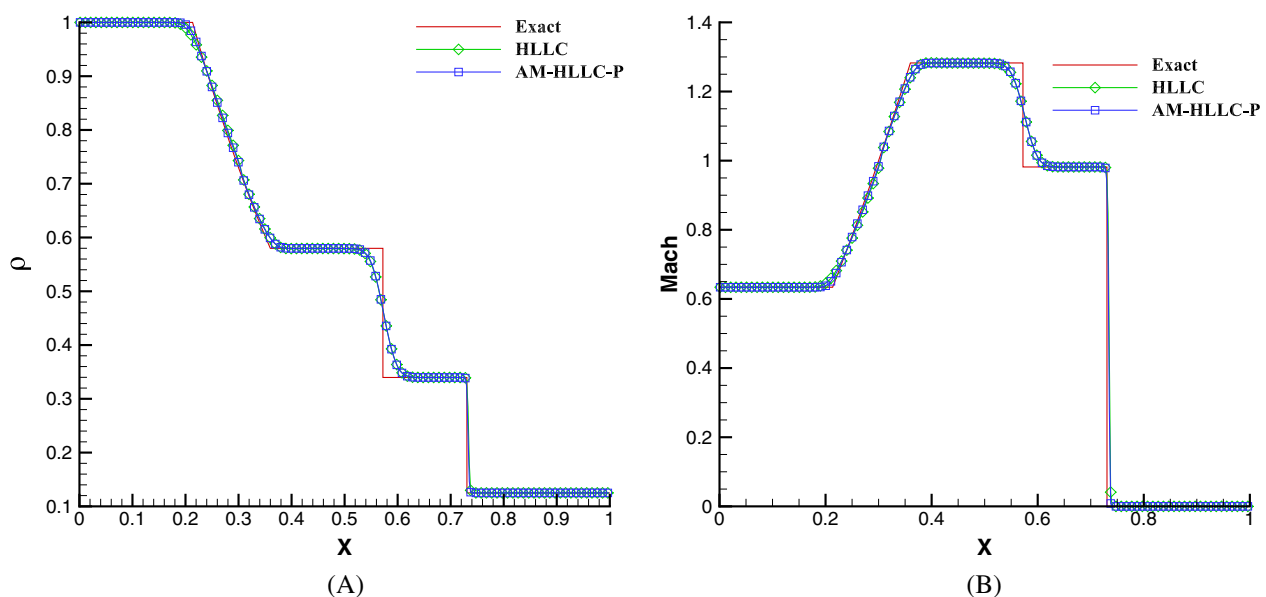


FIGURE 5 Modified Sod's shock tube problem at time $t = 0.2$ seconds. A, Density profiles; B, Mach number profiles (only a quarter of symbols is shown for clarity) [Colour figure can be viewed at wileyonlinelibrary.com]

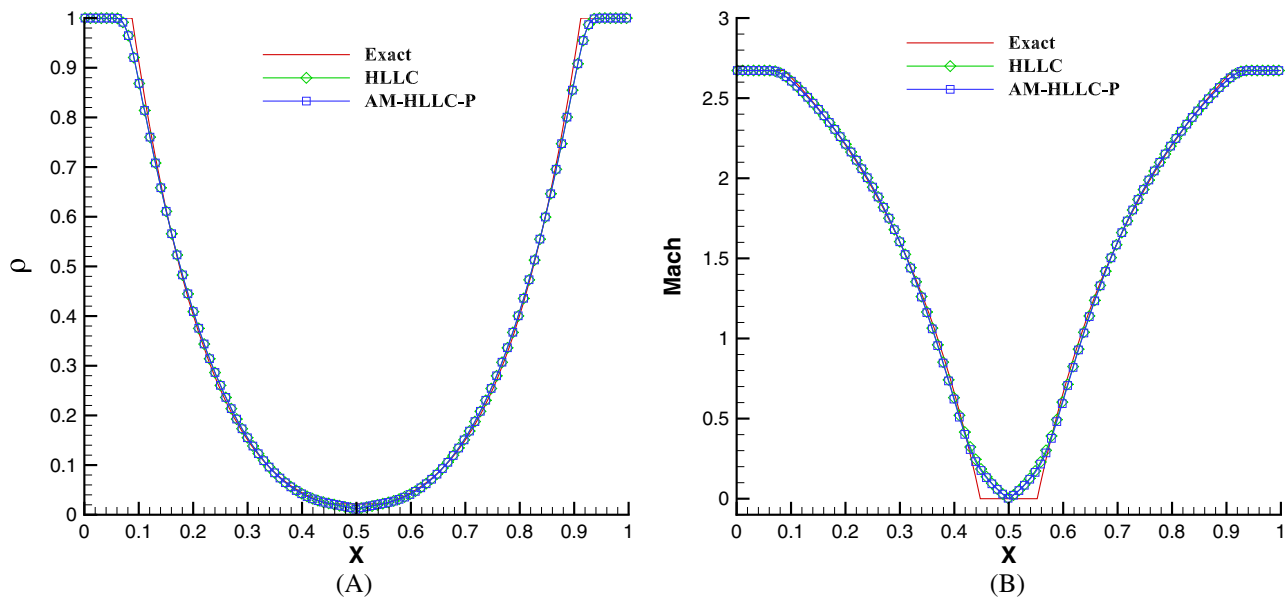


FIGURE 6 A vacuum test problem at time $t = 0.15$ seconds. A, Density profiles; B, Mach number profiles (only a quarter of symbols are shown for clarity) [Colour figure can be viewed at wileyonlinelibrary.com]

for the AM-HLLC-P solver are almost the same as that of the HLLC scheme, they show a correct agreement with the exact solution. Both schemes are able to preserve the positivity of the solution.

6.3 | Mach 20 hypersonic inviscid flow past a cylinder

This is a well-known test to assess the performance of an approximate Riemann solver with respect to the catastrophic carbuncle failings. A cylinder with a radius of the reference length is located in a uniform gas where the upstream Mach number is set as 20. The axis of the cylinder is at the origin $(x, y) = (0, 0)$. The following mesh system⁵⁴ is used to define and discrete the computational domain

$$\begin{aligned}\bar{x} &= -(3.8 - 2.8\xi) \cos \eta, \\ \bar{y} &= (3.8 - 2.8\xi) \sin \eta, \\ \frac{1}{2} &\leq \xi \leq 1, -\frac{2\pi}{5} \leq \eta \leq \frac{2\pi}{5},\end{aligned}\tag{73}$$

where the spatial coordinates are normalized by the radius of the cylinder and the intervals for ξ and η are uniformly divided into 180 and 240 sections. The computational domain has been initialized with values $\rho = 1.4$, $p = 1$, $u = 20$, and $v = 0$. At the wall, the slip condition is used and the other two are taken as outflow. Simulations are conducted in first-order accurate schemes and the two-stage Runge-Kutta explicit time-stepping scheme with $CFL = 0.5$.

In Figure 7, the density contours computed by HLLC and AM-HLLC-P schemes are illustrated, where 20 contour levels varying from 2.0 to 8.0 are used. The computational result from the HLLC scheme is taken as a reference solution due to its reliability and robustness in capturing strong shocks. As shown in Figure 7, the HLLC scheme exhibits the carbuncle phenomenon, appreciable postshock wrinkles are visible. However, the AM-HLLC-P scheme produces a clean shock profile and its postshock region is free from any shock anomalies. It shows a fairly high level of robustness as that of the HLLC scheme.

6.4 | Double Mach reflection problem

To further assess the performance of the proposed HLLC-type scheme for strong shocks, we consider the double Mach reflection problem. In contrast to the above cylinder case, this test case is an unsteady problem. It is extensively studied by Woodward and Colella⁵⁵ and followed by many other scholars for the inviscid flow. The problem describes a planar shock wave propagating in inviscid fluid, which is reflected by a 30° ramp. The computational domain is $[0, 4] \times [0, 1]$, which has been divided into 960 cells along the length and 240 cells along the width. The shock wave has a strength with Mach number 10, which is initially set up to be inclined at an angle of 60° with the bottom reflecting wall. The domain in front

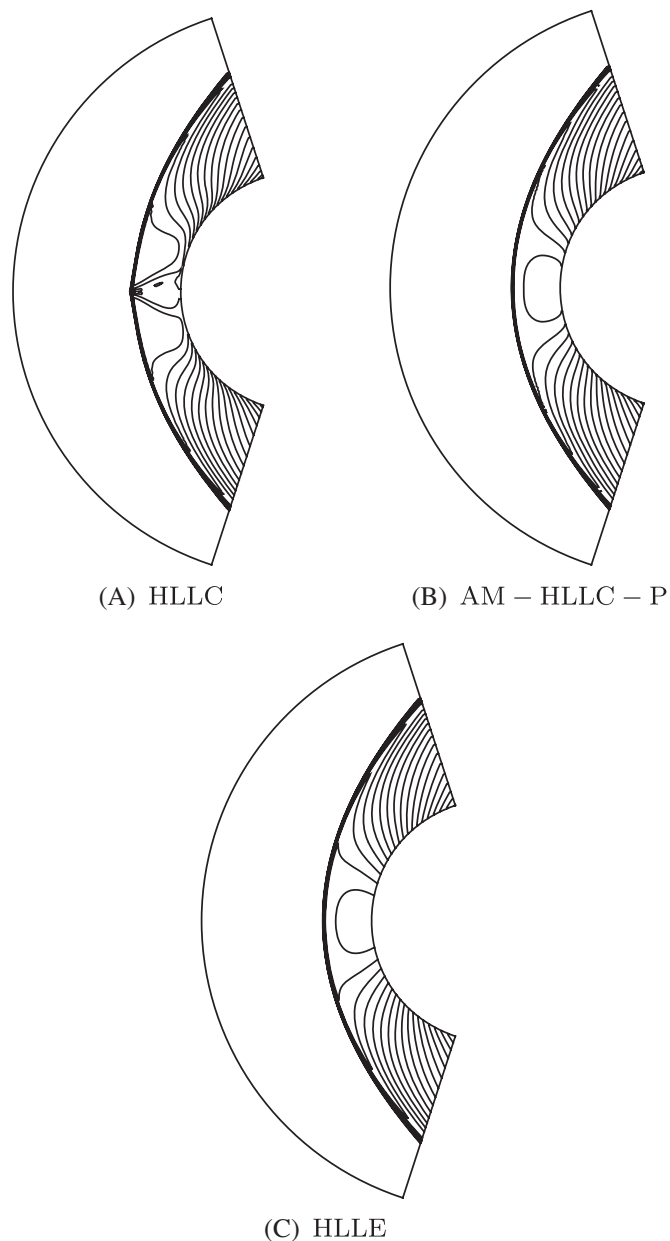


FIGURE 7 The density contours for hypersonic flow over a cylinder. A, HLLC; B, AM-HLLC-P; C, HLLE

of the shock is initialized with preshock values given as $\rho = 1.4, u = 0, v = 0, p = 1$. The domain behind the shock is initialized to post shock values. At the top boundary, the flow variables are set to describe the exact motion of the shock front along the wall. The inflow and outflow boundary conditions are used at the entrance and the exit.

The computations are performed by first-order numerical schemes and the third-order TVD Runge-Kutta time discretization⁵⁶ with CFL = 0.5 up to $t = 0.2$. The density contours computed by different schemes are shown in Figure 8, where 20 contour levels varying from 2.0 to 20.0 are used. As shown, the HLLC scheme produces a visible kinked Mach stem, demonstrating its vulnerability to shock instability. In contrast, the solutions from the AM-HLLC-P and HLLE schemes show no kinked Mach stems. Furthermore, the flow structure under the triple Mach stem is resolved clearly by the AM-HLLC-P method.

6.5 | Laminar boundary layer

To further demonstrate the ability of the proposed method to resolve shear layers accurately, a laminar boundary layer is tested over a flat plate with length $L = 100$. The freestream Mach number is $Ma = 0.3$ and the Reynolds number is

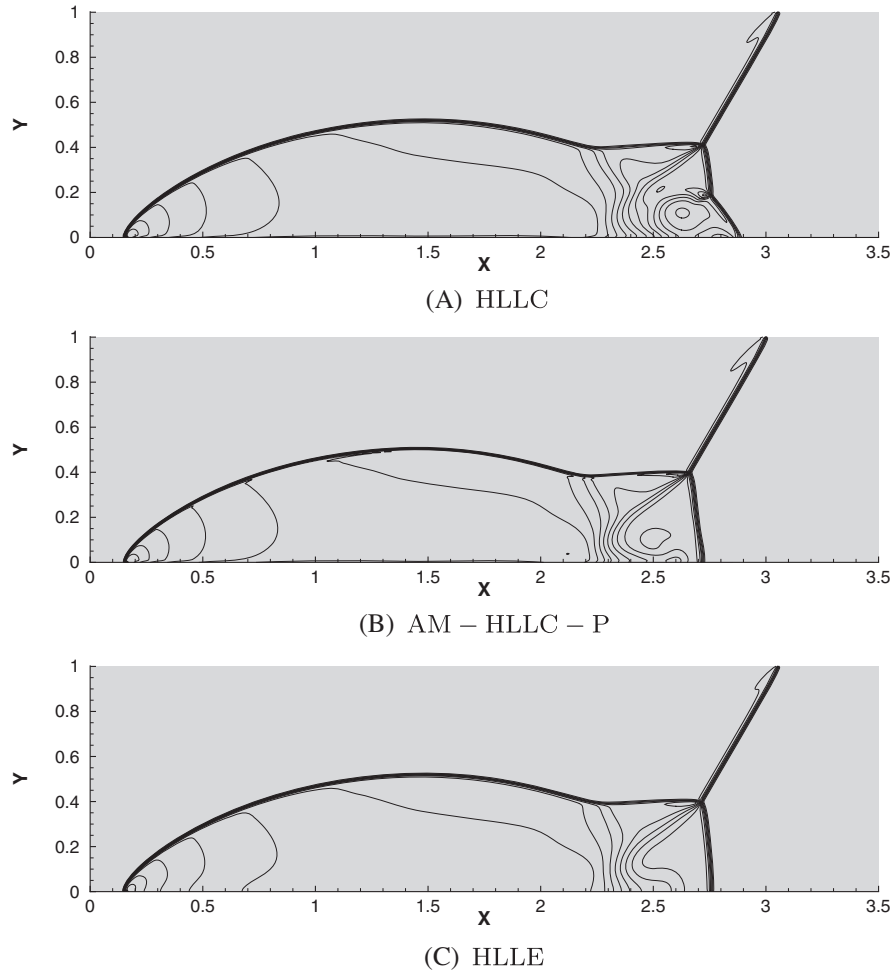


FIGURE 8 The density contours for double Mach reflection problem at $t = 0.2$

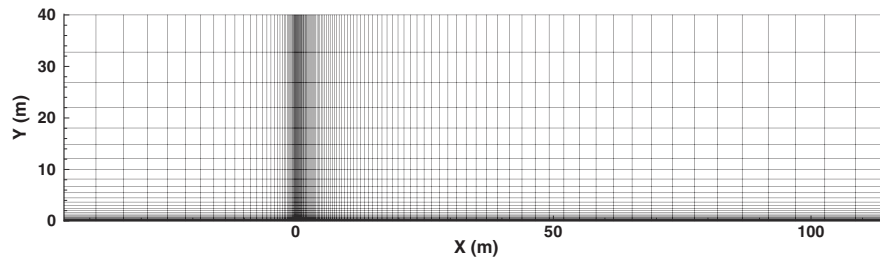


FIGURE 9 Computational mesh for the laminar boundary layer problem

$Re = U_{inf}L/\nu = 10^5$, ν is the viscous coefficient. This problem is simulated using a second-order Navier-Stokes code for a rectangular mesh with 120×30 nonuniform grid points. Figure 9 presents the computational mesh. As shown, the nonslip adiabatic boundary condition is imposed at the plate and a symmetry condition is used at the bottom boundary before the flat plate. The nonreflecting boundary condition based on the Riemann invariants is adopted for other boundaries. The computations were conducted for 50 000 steps using the two-stage Runge-Kutta explicit time-stepping scheme with $CFL = 0.5$, and all the computations achieved at least three orders of magnitude reductions of the density residuals. The results of different schemes are compared in Figure 10, as well as Blasius' analytical solution for a laminar boundary layer. As shown, the proposed scheme AM-HLLC-P can successfully reproduce the analytical velocity profile just as the HLLC scheme does. The result of the HLLE scheme is also included in Figure 10 for comparison. As expected, the HLLE scheme produces a very dissipative and inaccurate solution due to its dissipative property.

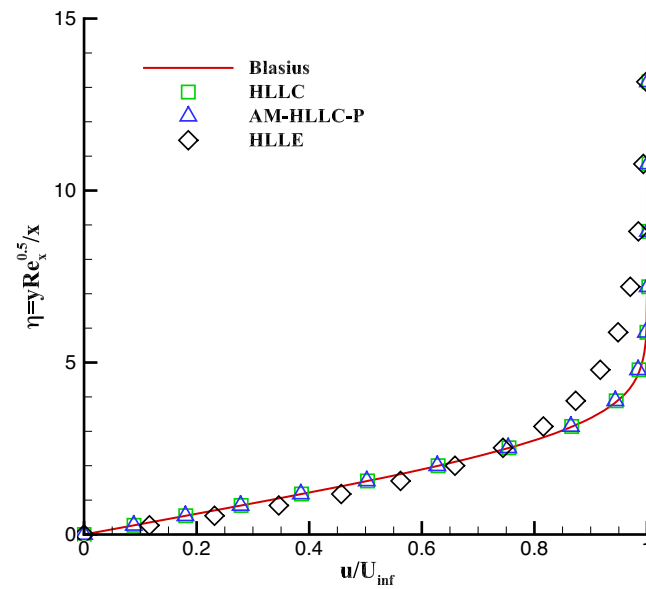
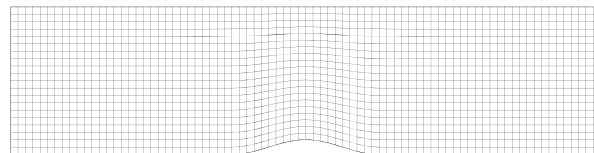
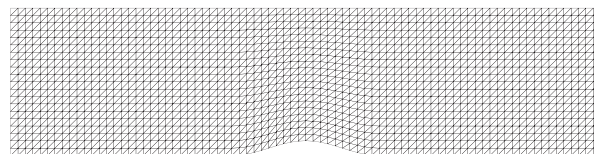


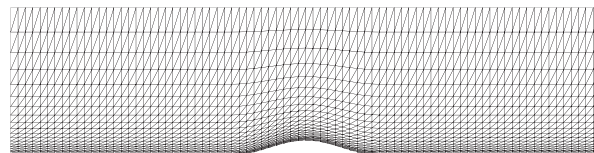
FIGURE 10 Nondimensional velocity profiles for the laminar boundary layer problem [Colour figure can be viewed at wileyonlinelibrary.com]



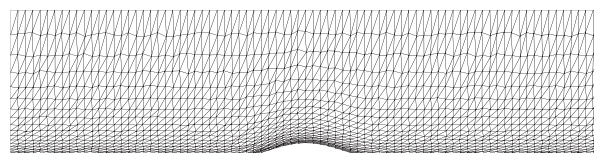
(A) Mesh – A



(B) Mesh – B



(C) Mesh – C



(D) Mesh – D

FIGURE 11 The mesh systems for the bump

6.6 | Channel with a bump

The flow in a channel with a circular arc bump^{33,57} is used to evaluate the presented HLLC-type method for computations of low Mach number steady state solutions. The bump in the 2D channel is defined by

$$y(x) = \begin{cases} \frac{1}{10} \cdot [1 - \cos((x-1)\pi)], & \text{if } x \in [1, 3], \\ 0, & \text{if } x \notin [1, 3]. \end{cases}$$

The computational domain is defined as $[0, 4] \times [0, 1]$, its top and bottom boundaries are discretized by 100 uniform cells, and the left and right boundaries are discretized by 25 uniform cells. In order to fully assess the robustness and accuracy of the proposed method in low Mach number regime, four types of computational grids are used. In Figure 11, we demonstrate these four mesh systems. To generate these meshes, we use the open code provided by Nishikawa.⁵⁸ As shown, mesh-A consists of 100×25 quadrangular cells, mesh-B consists of $100 \times 25 \times 2$ triangular cells which originate from Cartesian grid cells in mesh-A by introducing a diagonal. Mesh-C is obtained from mesh-B with a stretching in y -direction, and the mesh-D originates from mesh-C by perturbing the nodal coordinates to generate an irregular grid. The computational domain is initialized with conditions: $\rho_0 = 1.4, u_0 = M_0, v_0 = 0, p_0 = 1.0$, where the Mach number is set as $M_0 = 0.01$. Slip boundary conditions are used at upper and lower boundaries, and the values at left and right boundaries are defined by the flow at the infinity. Flow simulations are conducted using the HLLC and AM-HLLC-P schemes. All

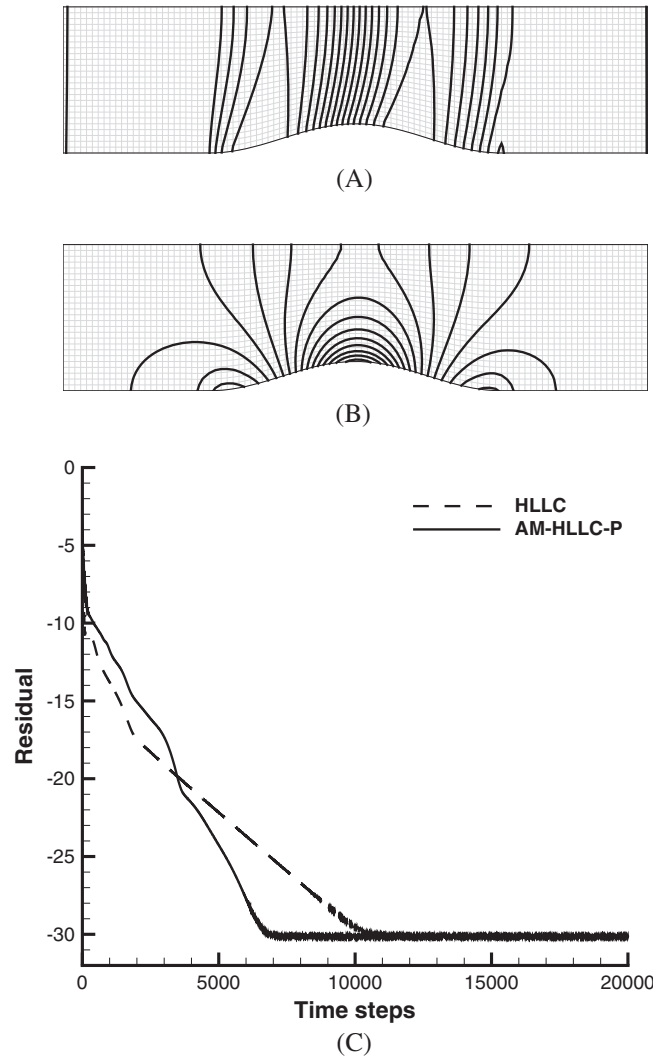


FIGURE 12 Computed pressure contours using the (A) HLLC and the (B) AM-HLLC-P schemes, (C) convergence histories from inviscid flow simulations in the bump at $M_0 = 0.01$

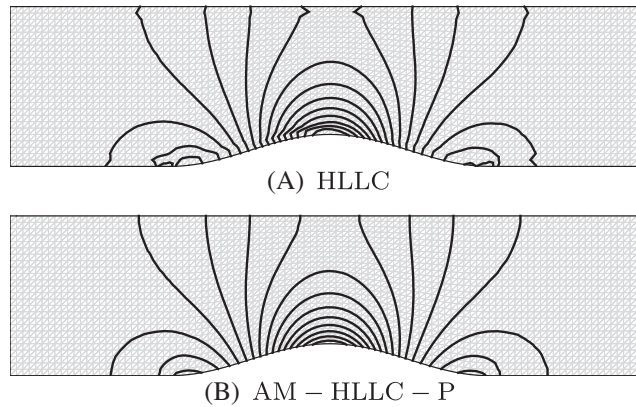


FIGURE 13 Computed pressure contours on mesh-B at $M_0 = 0.01$

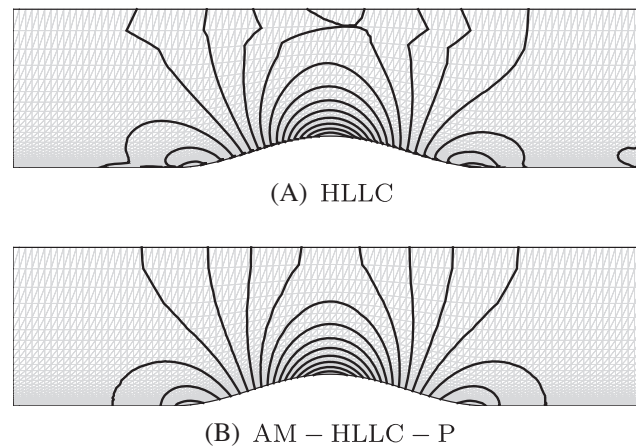


FIGURE 14 Computed pressure contours on mesh-C at $M_0 = 0.01$

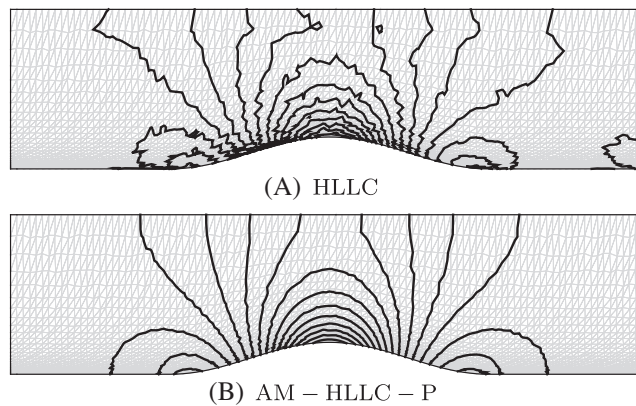


FIGURE 15 Computed pressure contours on mesh-D at $M_0 = 0.01$

the computations are conducted for 80 000 time steps with $CFL = 100$ using LU-SGS. The residuals (L2-norm of density) dropped at least ten orders of magnitude for most of the cases.

In Figure 12, computed results of the HLLC and AM-HLLC-P schemes on a quadrangular mesh (mesh-A) are demonstrated, where 15 contour levels varying from the minimal pressure to the maximal one are used. It can be observed that the solution given by the HLLC scheme is not correct. In contrast, the solution given by the AM-HLLC-P is close to the incompressible solution on a quadrangular mesh. The residual convergence histories show that the convergence rate of the AM-HLLC-P scheme is faster than that of the HLLC scheme. Solutions in Figures 13 to 15 demonstrate that the

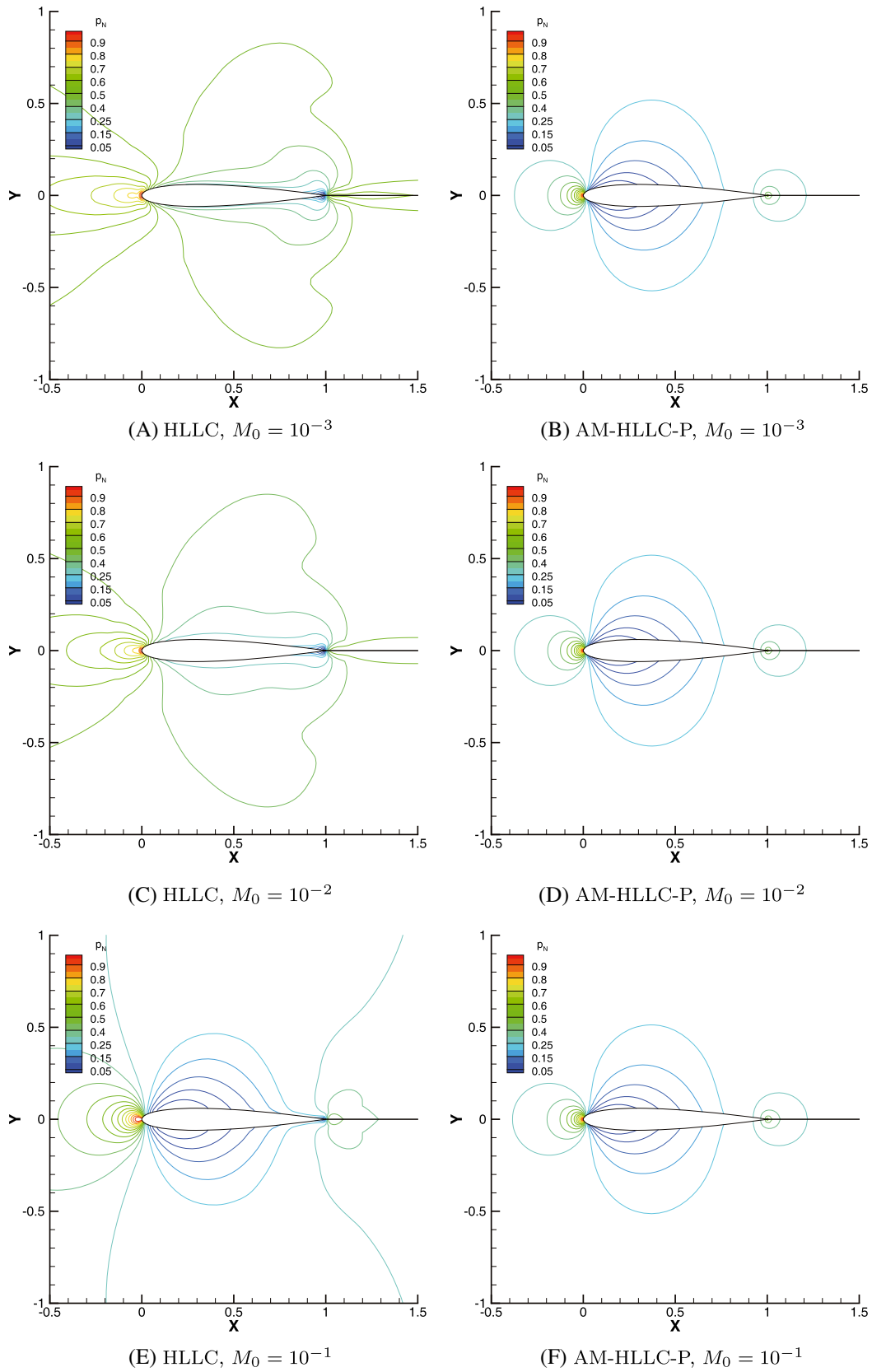


FIGURE 16 The normalized pressure fields for inviscid flows around NACA 0012 airfoil [Colour figure can be viewed at wileyonlinelibrary.com]

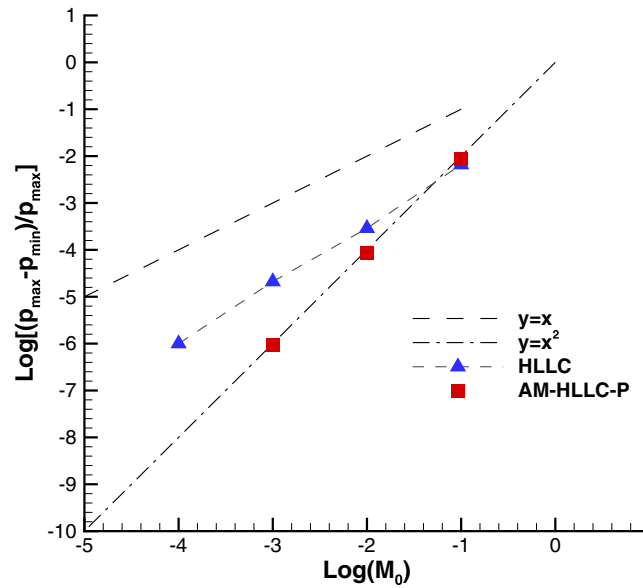


FIGURE 17 Pressure fluctuations with the inflow Mach number for the HLLC scheme and the AM-HLLC-P scheme [Colour figure can be viewed at wileyonlinelibrary.com]

AM-HLLC-P scheme does not suffer from any inaccuracy at low Mach number on triangular meshes, even with stretching and irregularity.

6.7 | Low Mach number inviscid flows around the NACA 0012 airfoil

The inviscid steady flow around the NACA 0012 airfoil is another typical test case to examine the performance of numerical schemes in the regime of low Mach number flow. An O-type mesh with 241 (circumferential) \times 121 (normal) cell number is used. The simulations are conducted at a zero angle of attack of three Mach numbers, $M_0 = 0.1, 0.01, 0.001$. All the computations are conducted for 50 000 time steps with CFL = 200 using LU-SGS. The residuals (L2-norm of density) dropped at least five orders of magnitude for all the cases. In Figure 16, we use a normalized pressure field²³ defined as $p_N = \frac{p(x,y) - p_{\min}}{p_{\max} - p_{\min}}$ to characterize the order of pressure fluctuations in the incompressible limit. It can be observed that the original HLLC scheme fails to simulate the low Mach number flows accurately, whereas the modified scheme converges to a solution that approaches the incompressible flow. Figure 17 shows the behavior of the pressure fluctuations with the inflow Mach number. As we know, first-order Riemann solvers for compressible flows usually support pressure fluctuations in space of order M_0 , whereas the physical pressure fluctuation should scale as M_0^2 . As shown in Figure 17, the original HLLC solver gives the incorrect scaling of the pressure fluctuations. With the improved HLLC-type scheme, the pressure fluctuations exactly scale with M_0^2 .

6.8 | Low Mach number turbulent flows around the NACA 0012 airfoil

In this test case, we continue to assess the performance of the proposed HLLC-type scheme in the low Mach number regime via the turbulent NACA 0012 airfoil case. The computational mesh is O-type with 241 (circumferential) \times 121 (normal) quadrilateral cells and the minimal mesh size near the airfoil surface is 1×10^{-6} C. The outer boundary is at 500C with the farfield boundary conditions. Flow conditions for this case are $M_0 = 0.1, 0.01, 0.001$, Reynolds number per chord is $Re = 6$ million, the angle of attack is zero. The proposed AM-HLLC-P scheme is used to compute the convective part of the Reynolds-averaged Navier-Stokes equations with SA model⁵⁹ for turbulence. All computations are conducted using LU-SGS approach with CFL = 5.0 for 100 000 time iterations. The residuals of mean-flow equations drop at least ten orders of magnitude for all the cases. The computed results are compared with the experimental data⁶⁰ in Figure 18. As shown, all the computed surface pressures are in good agreement with the experiment data, demonstrating its accuracy for essentially incompressible flows.

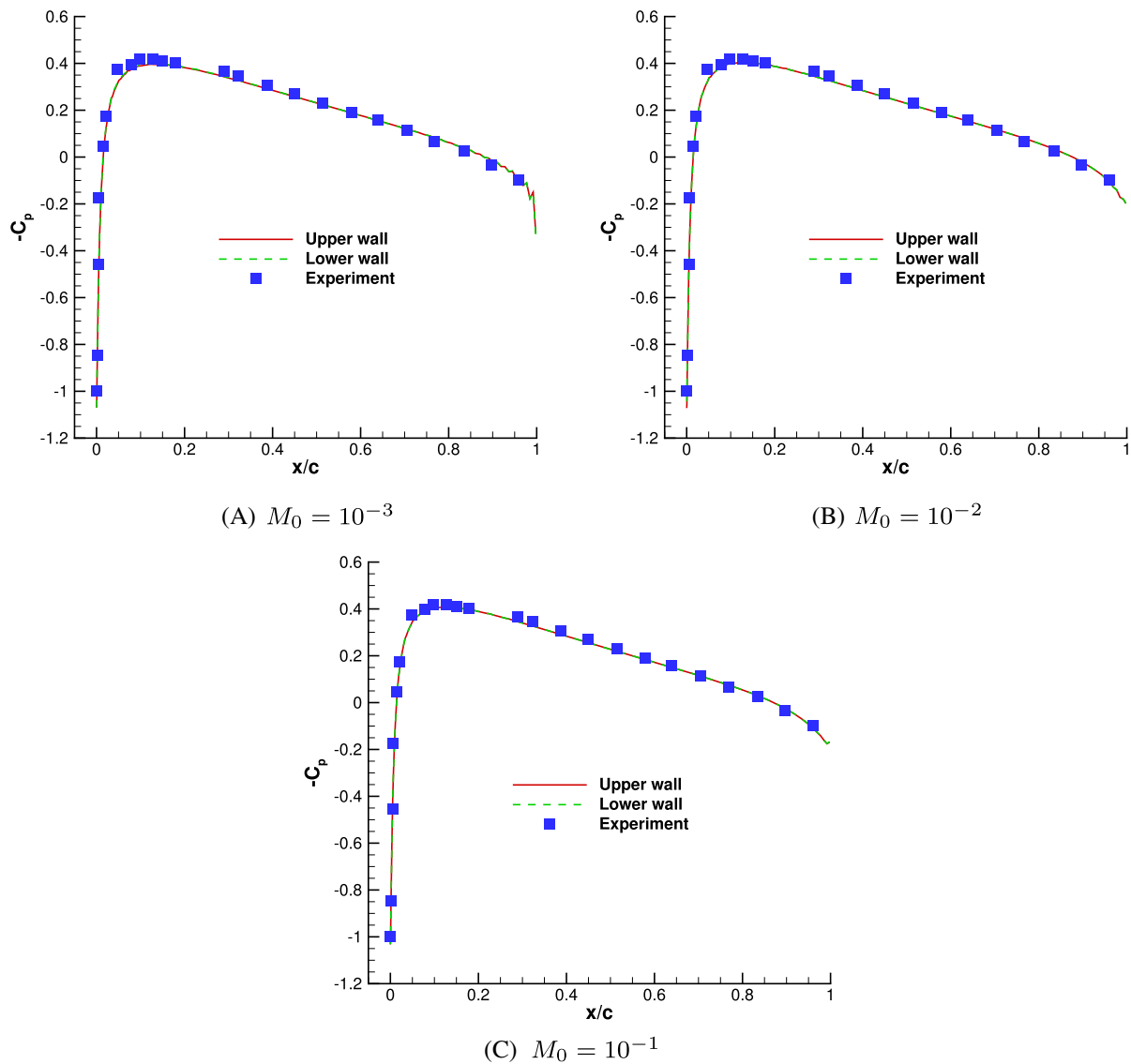


FIGURE 18 Surface pressure coefficient C_p for NACA 0012 airfoil [Colour figure can be viewed at wileyonlinelibrary.com]

6.9 | RAE 2822 transonic airfoil

To assess the smooth transition of the all Mach HLLC-type scheme with the original HLLC scheme at the sonic line and the effect of the all Mach correction term at the stagnation point, we consider here viscous turbulent flows over RAE 2822 airfoil at the transonic regime.⁶¹ The freestream Mach number is set as 0.729 at an angle of attack of 2.31° , and the freestream static temperature is 460.0R. These conditions correspond to a Reynolds number of 6.5 million based on the chord length. The static pressure can be computed based on the specified Reynolds number, Mach number, and the static temperature. The Reynolds-averaged Navier-Stokes equations are used to model the flow. The computational mesh is a structured O-type grid with dimensions of 369 (circumferential) \times 165 (normal) and the minimal mesh size near the airfoil surface is $1 \times 10^{-5}C$. The outer boundary is at 200C with the farfield boundary conditions. Flow simulations are conducted using the HLLC and the AM-HLLC-P schemes according to the experimental conditions. The second MUSCL reconstruction with minmod limiter and SA turbulence model⁵⁹ is employed. We use the implicit LU-SGS approach with CFL=5 for 100 000 time iterations. A convergence criterion of ten orders of magnitude reduction of the mean-flow equations residual is used.

In Figure 19, the Mach number isolines are shown. It can be observed that the superimposed solutions of the original HLLC and AM-HLLC-P schemes are hardly distinguishable. In Figure 20, surface pressure coefficients computed by both HLLC-type schemes are compared with the experimental data. As shown, the AM-HLLC-P scheme resolves the smooth

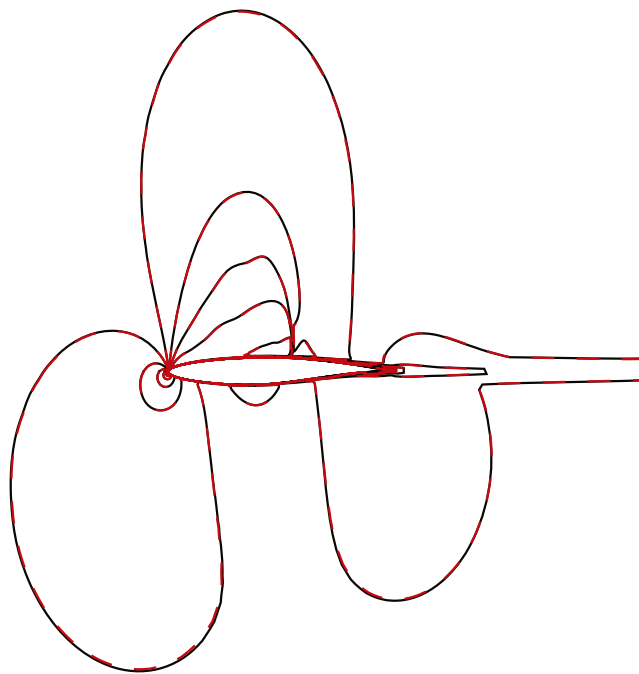


FIGURE 19 Mach number isolines for RAE 2822 airfoil (12 equally spaced levels from 0.1 to 1.2). HLLC (black solid line) and AM-HLLC-P (red dashed)

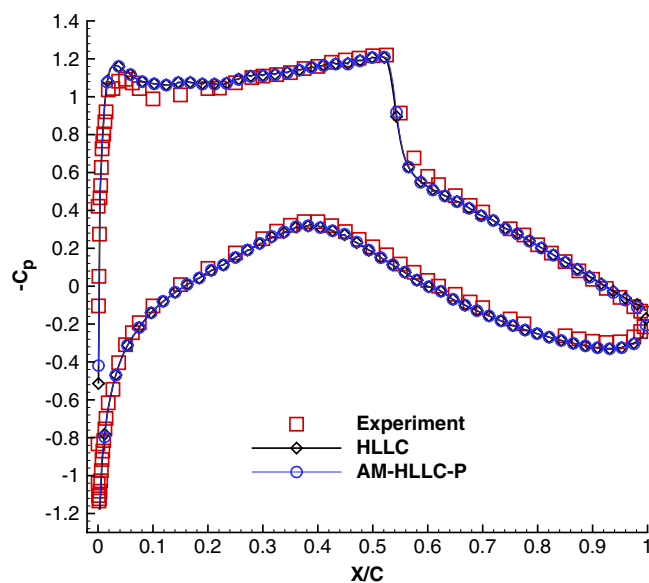


FIGURE 20 Surface pressure coefficient C_p for RAE 2822 airfoil

surface pressure coefficient profiles well and there is no any significant difference between the numerical results. They are in good agreement with the experimental data.

7 | CONCLUSION

We have developed an all Mach HLLC-type scheme to apply to solve the compressible Euler equations at various Mach numbers. In contrast to the original HLLC scheme or other low dissipative Riemann solvers, the improved method is endowed with a high level of robustness against shock instability while preserving sharp capturing of different kinds of discontinuities. The robustness of the HLLC scheme against strong shocks is improved via the introduction of a

pressure-control technique. It plays a role in damping erroneous pressure perturbation at shocks and limiting its propagation from inside the numerical shock structure to the downstream region. To remove the accuracy problem of the HLLC scheme in the low Mach number regime, a simple all Mach correction proposed in the work of Dellacherie et al³⁴ is applied to the HLLC-type Riemann solver. The resulting all Mach HLLC-type scheme is able to maintain solution accuracy and efficiency for computations of flows at all speeds. The proposed all Mach HLLC-type scheme outperforms other low Mach extensions of the HLLC scheme, because it will not suffer from shock anomalies, such as the carbuncle phenomenon, in simulations of high speed flows. In conclusion, the proposed HLLC-type Riemann solver is attractive due to its favorable properties and could also be extended to deal with the two-phase compressible flow model, which is applied in simulations of liquid-gas flows.

ACKNOWLEDGEMENTS

This work was supported by the National Natural Science Foundation of China (Grant 11472004) and the Foundation of Innovation of National University of Defense Technology (Grant B150106). The authors would like to thank the anonymous referees for their helpful comments which helped to improve the quality of this paper.

ORCID

Wenjia Xie  <https://orcid.org/0000-0003-4664-7996>

REFERENCES

1. Toro EF, Spruce M, Speares W. Restoration of the contact surface in the HLL-Riemann solver. *Shock Waves*. 1994;4(1):25-34. <https://doi.org/10.1007/BF01414629>
2. Roe PL. Approximate Riemann solvers, parameter vectors, and difference schemes. *J Comput Phys*. 1981;43(2):357-372. [https://doi.org/10.1016/0021-9991\(81\)90128-5](https://doi.org/10.1016/0021-9991(81)90128-5)
3. Osher S, Solomon F. Upwind difference schemes for hyperbolic systems of conservation laws. *Math Comput*. 1982;38(158):339-374. <https://doi.org/10.1090/S0025-5718-1982-0645656-0>
4. Harten A, Lax PD, van Leer B. On upstream differencing and Godunov-type schemes for hyperbolic conservation laws. *SIAM Rev*. 1983;25(1):35-61. <https://doi.org/10.1137/1025002>
5. Batten P, Leschziner M, Goldberg U. Average-state Jacobians and implicit methods for compressible viscous and turbulent flows. *J Comput Phys*. 1997;137(1):38-78. <https://doi.org/10.1006/jcph.1997.5793>
6. Mignone A, Bodo G. An HLLC Riemann solver for relativistic flows—II. Magnetohydrodynamics. *Mon Notices Royal Astron Soc*. 2006;368(3):1040-1054. <https://doi.org/10.1111/j.1365-2966.2006.10162.x>
7. Gurski KF. An HLLC approximate Riemann solver for ideal magnetohydrodynamics. *SIAM J Sci Comput*. 2004;25(6):2165-2187. <https://doi.org/10.1137/S1064827502407962>
8. Tokareva SA, Toro EF. HLLC-type Riemann solver for the Baer-Nunziato equations of compressible two-phase flow. In: Computational Fluid Dynamics 2010—Proceedings of the 6th International Conference on Computational Fluid Dynamics, ICCFD; 2011; St Petersburg, Russia. https://doi.org/10.1007/978-3-642-17884-9_10
9. Furfaro D, Saurel R. A simple HLLC-type Riemann solver for compressible non-equilibrium two-phase flows. *Comput Fluids*. 2015;111:159-178. <http://libyc.nudt.edu.cn:8000/rwt/ELSEVIER/> <https://doi.org/10.1016/j.compfluid.2015.01.016>
10. Peery K, Inlay S. Blunt-body flow simulations. In: 24th Joint Propulsion Conference, Joint Propulsion Conferences, American Institute of Aeronautics and Astronautics; 1988; Boston, MA. <https://doi.org/10.2514/6.1988-2904>
11. Quirk JJ. A contribution to the great Riemann solver debate. *Int J Numer Methods Fluids*. 1994;18(6):555-574.
12. Einfeldt B. On Godunov-type methods for gas dynamics. *SIAM J Numer Anal*. 1988;25(2):294-318.
13. Chauvat Y, Moschetta J-M, Gressier J. Shock wave numerical structure and the carbuncle phenomenon. *Int J Numer Meth Fluid*. 2005;47:903-909.
14. Kim SD, Lee BJ, Lee HJ, Jeung IS, Choi JY. Realization of contact resolving approximate Riemann solvers for strong shock and expansion flows. *Int J Numer Methods Fluids*. 2010;62(10):1107-1133.
15. Huang K, Wu H, Yu H, Yan D. Cures for numerical shock instability in HLLC solver. *Int J Numer Methods Fluids*. 2011;65(9):1026-1038.
16. Hu LJ, Yuan L. A robust hybrid HLLC-FORCE scheme for curing numerical shock instability. *Appl Mech Mater*. 2014;577. <https://doi.org/10.4028/www.scientific.net/AMM.577.749>
17. Gao ZX, Xue HC, Zhang ZC, Liu HP, Lee CH. A hybrid numerical scheme for aeroheating computation of hypersonic reentry vehicles. *Int J Heat Mass Transf*. 2018;116:432-444. <https://doi.org/10.1016/j.ijheatmasstransfer.2017.07.100>
18. Shen Z, Yan W, Yuan G. A stability analysis of hybrid schemes to cure shock instability. *Commun Comput Phys*. 2014;15(5):1320-1342. <https://doi.org/10.4208/cicp.210513.091013a>
19. Shen Z, Yan W, Yuan G. A robust HLLC-type Riemann solver for strong shock. *J Comput Phys*. 2016;309:185-206. <https://doi.org/10.1016/j.jcp.2016.01.001>

20. Rodionov AV. Artificial viscosity in Godunov-type schemes to cure the carbuncle phenomenon. *J Comput Phys*. 2017;345:308-329. <https://doi.org/10.1016/j.jcp.2017.05.024>
21. Xie W, Li W, Li H, Tian Z, Pan S. On numerical instabilities of Godunov-type schemes for strong shocks. *J Comput Phys*. 2017;350:607-637. <https://doi.org/10.1016/J.JCP.2017.08.063>
22. Volpe G. Performance of compressible flow codes at low Mach numbers. *AIAA J*. 1993;31(1):49-56. <https://doi.org/10.2514/3.11317>
23. Guillard H, Viozat C. On the behaviour of upwind schemes in the low Mach number limit. *Comput Fluids*. 1999;28(1):63-86. [https://doi.org/10.1016/S0045-7930\(98\)00017-6](https://doi.org/10.1016/S0045-7930(98)00017-6)
24. Guillard H, Murrone A. On the behavior of upwind schemes in the low Mach number limit: II. Godunov type schemes. *Comput Fluids*. 2004;33(4):655-675. <https://doi.org/10.1016/j.compfluid.2003.07.001>
25. Turkel E. Preconditioned methods for solving the incompressible and low speed compressible equations. *J Comput Phys*. 1987;72(2):277-298. [https://doi.org/10.1016/0021-9991\(87\)90084-2](https://doi.org/10.1016/0021-9991(87)90084-2)
26. Boniface JC. Rescaling of the Roe scheme in low Mach-number flow regions. *J Comput Phys*. 2017;328:177-199.
27. Li XS, Gu CW. An all-speed Roe-type scheme and its asymptotic analysis of low Mach number behaviour. *J Comput Phys*. 2008;227(10):5144-5159. <https://doi.org/10.1016/j.jcp.2008.01.037>
28. Li XS, Gu CW, Xu JZ. Development of Roe-type scheme for all-speed flows based on preconditioning method. *Comput Fluids*. 2009;38(4):810-817. <https://doi.org/10.1016/j.compfluid.2008.08.002>
29. Li XS, Gu CW. Mechanism of Roe-type schemes for all-speed flows and its application. *Comput Fluids*. 2013;86:56-70. <https://doi.org/10.1016/j.compfluid.2013.07.004>
30. Rieber F. A low-Mach number fix for Roe's approximate Riemann solver. *J Comput Phys*. 2011;230(13):5263-5287. <https://doi.org/10.1016/j.jcp.2011.03.025>
31. Thornber B, Drikakis D, Williams R, Youngs D. On entropy generation and dissipation of kinetic energy in high-resolution shock-capturing schemes. *J Comput Phys*. 2008;227(10):4853-4872. <https://doi.org/10.1016/j.jcp.2008.01.035>
32. Rieber F, Bader G. The influence of cell geometry on the accuracy of upwind schemes in the low Mach number regime. *J Comput Phys*. 2009;228(8):2918-2933. <https://doi.org/10.1016/j.jcp.2009.01.002>
33. Dellacherie S. Analysis of Godunov type schemes applied to the compressible Euler system at low Mach number. *J Comput Phys*. 2010;229(4):978-1016.
34. Dellacherie S, Jung J, Omnes P, Raviart P-A. Construction of modified Godunov-type schemes accurate at any Mach number for the compressible Euler system. *Math Models Methods Appl Sci*. 2016;26(13):2525-2615. <https://doi.org/10.1142/S0218202516500603>
35. Liou M-S. A sequel to AUSM, part II: AUSM+-up for all speeds. *J Comput Phys*. 2006;214(1):137-170. <https://doi.org/10.1016/j.jcp.2005.09.020>
36. Fillion P, Chanoine A, Dellacherie S, Kumbaro A. FLICA-OVAP: a new platform for core thermal-hydraulic studies. *Nucl Eng Des*. 2011;241(11):4348-4358. Part of special issue: 13th International Topical Meeting on Nuclear Reactor Thermal Hydraulics (NURETH-13). <https://doi.org/10.1016/j.nucengdes.2011.04.048>
37. Oßwald K, Siegmund A, Birken P, Hannemann V, Meister A. L2Roe: a low dissipation version of Roe's approximate Riemann solver for low Mach numbers. *Int J Numer Methods Fluids*. 2016;81(2):71-86. <http://arxiv.org/abs/fld.1> <https://doi.org/10.1002/fld.4175>
38. Luo H, Baum JD, Lohner R. Extension of Harten-Lax-van Leer scheme for flows at all speeds. *AIAA J*. 2005;43(6):1160-1166. <https://doi.org/10.2514/1.7567>
39. Gupta A. *Preconditioning Methods for Ideal and Multiphase Fluid Flows* [PhD thesis]. Chattanooga, TN: University of Tennessee at Chattanooga; 2013. <https://scholar.utc.edu/theses/279>
40. Gupta A, Sreenivas K, Taylor LK. Preconditioning methods for multiphase flows. Paper presented at: 11th AIAA/ASME Joint Thermophysics and Heat Transfer Conference; 2014; Atlanta, GA.
41. Pelanti M. Low Mach number preconditioning techniques for Roe-type and HLLC-type methods for a two-phase compressible flow model. *Appl Math Comput*. 2017;310:112-133. <https://doi.org/10.1016/j.amc.2017.04.014>
42. Toro EF. *Riemann Solvers and Numerical Methods for Fluid Dynamics: A Practical Introduction*. Berlin, Germany: Springer Science & Business Media; 2013.
43. Davis S. Simplified second-order Godunov-type methods. *SIAM J Sci Stat Comput*. 1988;9(3):445-473. <https://doi.org/10.1137/0909030>
44. Einfeldt B, Munz C, Roe P, Sjogreen B. On Godunov-type methods near low densities. *J Comput Phys*. 1991;92(2):273-295. [https://doi.org/10.1016/0021-9991\(91\)90211-3](https://doi.org/10.1016/0021-9991(91)90211-3)
45. Dumbser M, Moschetta J-M, Gressier J. A matrix stability analysis of the carbuncle phenomenon. *J Comput Phys*. 2004;197(2):647-670.
46. Chen SS, Yan C, Lin B-X, Li Y-S. A new robust carbuncle-free Roe scheme for strong shock. *J Sci Comput*. 2018;1-28.
47. Agrawal A, Srinivasan B. Stability analysis of the carbuncle phenomenon and the sonic point glitch. *Sādhanā*. 2017;42(5):741-757.
48. Simon S, Mandal J. A cure for numerical shock instability in HLLC Riemann solver using antidiffusion control. *Comput Fluids*. 2018;174:144-166. <https://doi.org/10.1016/j.compfluid.2018.07.001>
49. Thornber B, Mosedale A, Drikakis D, Youngs D, Williams R. An improved reconstruction method for compressible flows with low Mach number features. *J Comput Phys*. 2008;227(10):4873-4894. <https://doi.org/10.1016/j.jcp.2008.01.036>
50. Shima E, Kitamura K. Parameter-free simple low-dissipation AUSM-family scheme for all speeds. *AIAA J*. 2011;49(8):1693-1709.
51. Chen SS, Yan C, Xiang XH. Effective low-Mach number improvement for upwind schemes. *Comput Math Appl*. 2018;75(10):3737-3755. <https://doi.org/10.1016/j.camwa.2018.02.028>

52. Batten P, Clarke N, Lambert C, Causon DM. On the choice of wavespeeds for the HLLC Riemann solver. *SIAM J Sci Comput*. 1997;18(6):1553-1570.
53. Sod GA. A survey of several finite difference methods for systems of nonlinear hyperbolic conservation laws. *J Comput Phys*. 1978;27(1):1-31. [https://doi.org/10.1016/0021-9991\(78\)90023-2](https://doi.org/10.1016/0021-9991(78)90023-2)
54. Ohwada T, Adachi R, Xu K, Luo J. On the remedy against shock anomalies in kinetic schemes. *J Comput Phys*. 2013;255:106-129. <https://doi.org/10.1016/j.jcp.2013.07.038>
55. Woodward P, Colella P. The numerical simulation of two-dimensional fluid flow with strong shocks. *J Comput Phys*. 1984;54(1):115-173. [https://doi.org/10.1016/0021-9991\(84\)90142-6](https://doi.org/10.1016/0021-9991(84)90142-6)
56. Shu C-W, Osher S. Efficient implementation of essentially non-oscillatory shock-capturing schemes. *J Comput Phys*. 1988;77(2):439-471. [https://doi.org/10.1016/0021-9991\(88\)90177-5](https://doi.org/10.1016/0021-9991(88)90177-5)
57. Vidović D, Segal A, Wesseling P. A superlinearly convergent Mach-uniform finite volume method for the Euler equations on staggered unstructured grids. *J Comput Phys*. 2006;217(2):277-294.
58. Nishikawa H. Free CFD codes. <http://www.ossanworld.com/cfdbooks/cfdcodes.html/>
59. Spalart P, Allmaras S. A one-equation turbulence model for aerodynamic flows. Paper presented at: 30th Aerospace Sciences Meeting and Exhibit, Aerospace Sciences Meetings; 1992; Reno, NV.
60. Gregory N. Low-speed aerodynamic characteristics of NACA0012 aerofoil section, including the effects of upper-surface roughness simulating hoar frost. 1970. ARC R&M (3726).
61. Cook P, McDonald M, Firmin M. Aerofoil RAE 2822—Pressure Distributions, and Boundary Layer and Wake Measurements. 1979. AGARD Advisory Report 138.

How to cite this article: Xie W, Zhang R, Lai J, Li H. An accurate and robust HLLC-type Riemann solver for the compressible Euler system at various Mach numbers. *Int J Numer Meth Fluids*. 2019;89:430–463. <https://doi.org/10.1002/fld.4704>

APPENDIX A

A.1 | Asymptotic equations of the AM-HLLC-P scheme

To derive the asymptotic equations of the AM-HLLC-P scheme, we consider now the left star flux, with the corresponding results for the right star flux following by symmetry. The explicit equations for the transport of density ρ , momentum density ρu and ρv , and the density of total energy ρe are given by

$$A_i \frac{d}{dt} \rho_i + \sum_{l \in v(i)} \frac{\rho_i a_i (\Delta_{il} p + \rho_i a_i q_i + \rho_l a_l q_l)}{\Delta_{il} p + \rho_i a_i^2 + \rho_l a_l (a_i - \Delta_{il} q)} \delta_{il} = 0 \quad (A1)$$

$$\begin{aligned} A_i \frac{d}{dt} \rho_i u_i + \sum_{l \in v(i)} \frac{\rho_i a_i (\Delta_{il} p + \rho_i a_i q_i + \rho_l a_l q_l)}{\Delta_{il} p + \rho_i a_i^2 + \rho_l a_l (a_i - \Delta_{il} q)} (u_i - (n_x)_{il} q_i) \delta_{il} \\ + \sum_{l \in v(i)} \frac{\rho_i a_i (\Delta_{il} p + \rho_i a_i q_i + \rho_l a_l q_l)}{\Delta_{il} p + \rho_i a_i^2 + \rho_l a_l (a_i - \Delta_{il} q)} \frac{\rho_i a_i q_i + \rho_l a_l q_l + \Delta_{il} p}{\rho_i a_i + \rho_l a_l} (n_x)_{il} \delta_{il} \\ + \sum_{l \in v(i)} \theta \frac{\rho_i a_i p_l + \rho_l a_l p_i + \rho_i a_i \rho_l a_l \Delta_{il} q}{\rho_i a_i + \rho_l a_l} (n_x)_{il} \delta_{il} + \sum_{l \in v(i)} (1 - \theta) \frac{p_i + p_l}{2} (n_x)_{il} \delta_{il} = 0 \end{aligned} \quad (A2)$$

$$\begin{aligned}
& A_i \frac{d}{dt} \rho_i v_i + \sum_{l \in v(i)} \frac{\rho_i a_i (\Delta_{il} p + \rho_i a_i q_i + \rho_l a_l q_l)}{\Delta_{il} p + \rho_i a_i^2 + \rho_l a_l (a_i - \Delta_{il} q)} (v_i - (n_y)_{il} q_i) \delta_{il} \\
& + \sum_{l \in v(i)} \frac{\rho_i a_i (\Delta_{il} p + \rho_i a_i q_i + \rho_l a_l q_l)}{\Delta_{il} p + \rho_i a_i^2 + \rho_l a_l (a_i - \Delta_{il} q)} \frac{\rho_i a_i q_i + \rho_l a_l q_l + \Delta_{il} p}{\rho_i a_i + \rho_l a_l} (n_y)_{il} \delta_{il} \\
& + \sum_{l \in v(i)} \theta \frac{\rho_i a_i p_l + \rho_l a_l p_i + \rho_i a_i \rho_l a_l \Delta_{il} q}{\rho_i a_i + \rho_l a_l} (n_y)_{il} \delta_{il} \\
& + \sum_{l \in v(i)} (1 - \theta) \frac{p_i + p_l}{2} (n_y)_{il} \delta_{il} = 0
\end{aligned} \tag{A3}$$

$$\begin{aligned}
& A_i \frac{d}{dt} \rho_i e_i + \sum_{l \in v(i)} \frac{\rho_i a_i (\rho_i a_i q_i + \rho_l a_l q_l + \Delta_{il} p) e_i}{a_i (\rho_i a_i + \rho_l a_l) - \rho_l a_l \Delta_{il} q + \Delta_{il} p} \delta_{il} \\
& + \sum_{l \in v(i)} \frac{(\rho_i a_i q_i + \rho_l a_l q_l + \Delta_{il} p) (\rho_i^2 a_i^2 q_i + \rho_i a_i \rho_l a_l q_l - \rho_i a_i p_l - \rho_l a_l p_i) (\Delta_{il} p - \rho_l a_l \Delta_{il} q)}{[a_i (\rho_i a_i + \rho_l a_l) - \rho_l a_l \Delta_{il} q + \Delta_{il} p] (\rho_i a_i + \rho_l a_l)^2} \delta_{il} \\
& + \sum_{l \in v(i)} \frac{(\rho_i a_i q_i + \rho_l a_l q_l + \Delta_{il} p) (\rho_i a_i p_l + \rho_l a_l p_i + \rho_i a_i \rho_l a_l \Delta_{il} q)}{(\rho_i a_i + \rho_l a_l)^2} \delta_{il} = 0,
\end{aligned} \tag{A4}$$

A.2 | Dimensional analysis

We use the same reference quantities as in the work of Rieper³⁰ to scale equations of the AM-HLLC-P scheme. In the following, all equations are sorted by orders of magnitude in M . The nondimensional form of the continuity equation is

$$M^0 \sum_{l \in v(i)} \frac{\rho_i a_i \Delta_{il} p}{\Delta_{il} p + \rho_i a_i^2 + \rho_l a_l a_i - M \rho_l a_l \Delta_{il} q} \delta_{il} + M^1 \left[A_i \frac{d}{dt} \rho_i + \sum_{l \in v(i)} \frac{\rho_i a_i (\rho_i a_i q_i + \rho_l a_l q_l)}{\Delta_{il} p + \rho_i a_i^2 + \rho_l a_l a_i - M \rho_l a_l \Delta_{il} q} \delta_{il} \right] = 0. \tag{A5}$$

A similar procedure leads to the equation of x -momentum conservation

$$\begin{aligned}
& M^{-1} \sum_{l \in v(i)} \frac{\rho_i a_i (\Delta_{il} p)^2 (n_x)_{il} + (\rho_i a_i + \rho_l a_l) \frac{p_i + p_l}{2} \Delta_{il} p (n_x)_{il} + a_i (\rho_i a_i + \rho_l a_l)^2 \frac{p_i + p_l}{2} (n_x)_{il}}{(\rho_i a_i + \rho_l a_l) \Delta_{il} p + a_i (\rho_i a_i + \rho_l a_l)^2 - \rho_l a_l (\rho_i a_i + \rho_l a_l) \Delta_{il} q \cdot M} \delta_{il} \\
& - M^0 \sum_{l \in v(i)} \left\{ \frac{\frac{1}{2} \Delta_{il} (\rho a) (\Delta_{il} p)^2 (n_x)_{il} + \frac{1}{2} a_i \Delta_{il} (\rho a) (\rho_i a_i + \rho_l a_l) \Delta_{il} p (n_x)_{il}}{(\rho_i a_i + \rho_l a_l) \Delta_{il} p + a_i (\rho_i a_i + \rho_l a_l)^2 - \rho_l a_l (\rho_i a_i + \rho_l a_l) \Delta_{il} q \cdot M} \right. \\
& - \frac{\rho_i a_i u_i (\rho_i a_i + \rho_l a_l) \Delta_{il} p - \rho_i a_i \rho_l a_l \Delta_{il} q \Delta_{il} p (n_x)_{il} + \rho_i a_i (\rho_i a_i q_i + \rho_l a_l q_l) \Delta_{il} p (n_x)_{il}}{(\rho_i a_i + \rho_l a_l) \Delta_{il} p + a_i (\rho_i a_i + \rho_l a_l)^2 - \rho_l a_l (\rho_i a_i + \rho_l a_l) \Delta_{il} q \cdot M} \\
& + \left. \frac{\frac{p_i + p_l}{2} \rho_l a_l (\rho_i a_i + \rho_l a_l) \Delta_{il} q (n_x)_{il}}{(\rho_i a_i + \rho_l a_l) \Delta_{il} p + a_i (\rho_i a_i + \rho_l a_l)^2 - \rho_l a_l (\rho_i a_i + \rho_l a_l) \Delta_{il} q \cdot M} \right\} \delta_{il} \\
& + M^1 \left\{ A_i \frac{d}{dt} (\rho_i u_i) + \sum_{l \in v(i)} \left\{ \frac{\frac{1}{2} \rho_l a_l \Delta_{il} (\rho a) \Delta_{il} p \Delta_{il} q (n_x)_{il} + \rho_i a_i \rho_l a_l \Delta_{il} p \Delta_{il} q (n_x)_{il}}{(\rho_i a_i + \rho_l a_l) \Delta_{il} p + a_i (\rho_i a_i + \rho_l a_l)^2 - \rho_l a_l (\rho_i a_i + \rho_l a_l) \Delta_{il} q \cdot M} \right. \right. \\
& + \left. \frac{\rho_i a_i^2 \rho_l a_l (\rho_i a_i + \rho_l a_l) \Delta_{il} q (n_x)_{il} + \rho_i a_i (\rho_i a_i q_i + \rho_l a_l q_l) [u_i (\rho_i a_i + \rho_l a_l) - (n_x)_{il} \rho_l a_l \Delta_{il} q]}{(\rho_i a_i + \rho_l a_l) \Delta_{il} p + a_i (\rho_i a_i + \rho_l a_l)^2 - \rho_l a_l (\rho_i a_i + \rho_l a_l) \Delta_{il} q \cdot M} \right\} \delta_{il} \\
& - M^2 \frac{\rho_i a_i (\rho_l a_l \Delta_{il} q)^2 (n_x)_{il}}{(\rho_i a_i + \rho_l a_l) \Delta_{il} p + a_i (\rho_i a_i + \rho_l a_l)^2 - \rho_l a_l (\rho_i a_i + \rho_l a_l) \Delta_{il} q \cdot M} \delta_{il} = 0,
\end{aligned} \tag{A6}$$

and the equation of y -momentum conservation

$$\begin{aligned}
& M^{-1} \sum_{i \in v(i)} \frac{\rho_i a_i (\Delta_{il} p)^2 (n_y)_{il} + (\rho_i a_i + \rho_l a_l) \frac{p_i + p_l}{2} \Delta_{il} p (n_y)_{il} + a_i (\rho_i a_i + \rho_l a_l)^2 \frac{p_i + p_l}{2} (n_y)_{il}}{(\rho_i a_i + \rho_l a_l) \Delta_{il} p + a_i (\rho_i a_i + \rho_l a_l)^2 - \rho_l a_l (\rho_i a_i + \rho_l a_l) \Delta_{il} q \cdot M} \delta_{il} \\
& - M^0 \sum_{i \in v(i)} \left\{ \frac{\frac{1}{2} \Delta_{il} (\rho a) (\Delta_{il} p)^2 (n_y)_{il} + \frac{1}{2} a_i \Delta_{il} (\rho a) (\rho_i a_i + \rho_l a_l) \Delta_{il} p (n_y)_{il}}{(\rho_i a_i + \rho_l a_l) \Delta_{il} p + a_i (\rho_i a_i + \rho_l a_l)^2 - \rho_l a_l (\rho_i a_i + \rho_l a_l) \Delta_{il} q \cdot M} \right. \\
& - \frac{\rho_i a_i u_i (\rho_i a_i + \rho_l a_l) \Delta_{il} p - \rho_i a_i \rho_l a_l \Delta_{il} q \Delta_{il} p (n_y)_{il} + \rho_i a_i (\rho_i a_i q_i + \rho_l a_l q_l) \Delta_{il} p (n_y)_{il}}{(\rho_i a_i + \rho_l a_l) \Delta_{il} p + a_i (\rho_i a_i + \rho_l a_l)^2 - \rho_l a_l (\rho_i a_i + \rho_l a_l) \Delta_{il} q \cdot M} \\
& + \left. \frac{\frac{p_i + p_l}{2} \rho_l a_l (\rho_i a_i + \rho_l a_l) \Delta_{il} q (n_y)_{il}}{(\rho_i a_i + \rho_l a_l) \Delta_{il} p + a_i (\rho_i a_i + \rho_l a_l)^2 - \rho_l a_l (\rho_i a_i + \rho_l a_l) \Delta_{il} q \cdot M} \right\} \delta_{il} \quad (A7) \\
& + M^1 \left\{ A_i \frac{d}{dt} (\rho_i u_i) + \sum_{i \in v(i)} \left\{ \frac{\frac{1}{2} \rho_l a_l \Delta_{il} (\rho a) \Delta_{il} p \Delta_{il} q (n_y)_{il} + \rho_i a_i \rho_l a_l \Delta_{il} p \Delta_{il} q (n_y)_{il}}{(\rho_i a_i + \rho_l a_l) \Delta_{il} p + a_i (\rho_i a_i + \rho_l a_l)^2 - \rho_l a_l (\rho_i a_i + \rho_l a_l) \Delta_{il} q \cdot M} \right. \right. \\
& + \left. \left. \frac{\rho_i a_i^2 \rho_l a_l (\rho_i a_i + \rho_l a_l) \Delta_{il} q (n_y)_{il} + \rho_i a_i (\rho_i a_i q_i + \rho_l a_l q_l) [u_i (\rho_i a_i + \rho_l a_l) - (n_y)_{il} \rho_l a_l \Delta_{il} q]}{(\rho_i a_i + \rho_l a_l) \Delta_{il} p + a_i (\rho_i a_i + \rho_l a_l)^2 - \rho_l a_l (\rho_i a_i + \rho_l a_l) \Delta_{il} q \cdot M} \right\} \right\} \delta_{il} \\
& - M^2 \frac{\rho_i a_i (\rho_l a_l \Delta_{il} q)^2 (n_y)_{il}}{(\rho_i a_i + \rho_l a_l) \Delta_{il} p + a_i (\rho_i a_i + \rho_l a_l)^2 - \rho_l a_l (\rho_i a_i + \rho_l a_l) \Delta_{il} q \cdot M} \delta_{il} = 0.
\end{aligned}$$

The equation of energy conservation in nondimensional form is

$$\begin{aligned}
& M^0 \sum_{i \in v(i)} \frac{\rho_i a_i h_i (\rho_i a_i + \rho_l a_l) \Delta_{il} p - \rho_i a_i^2 (\Delta_{il} p)^2}{(\rho_i a_i + \rho_l a_l) \Delta_{il} p + a_i (\rho_i a_i + \rho_l a_l)^2 - \rho_l a_l (\rho_i a_i + \rho_l a_l) \Delta_{il} q \cdot M} \delta_{il} \\
& + M^1 \left\{ A_i \frac{d}{dt} (\rho_i e_i) + \sum_{i \in v(i)} \left\{ \frac{\rho_i a_i q_i (\Delta_{il} p)^2 + [\rho_i a_i^2 \rho_l a_l \Delta_{il} q - \rho_i a_i^2 (\rho_l a_l q_l + \rho_i a_i q_i)] \Delta_{il} p}{(\rho_i a_i + \rho_l a_l) \Delta_{il} p + a_i (\rho_i a_i + \rho_l a_l)^2 - \rho_l a_l (\rho_i a_i + \rho_l a_l) \Delta_{il} q \cdot M} \right. \right. \\
& + \left. \left. \frac{\rho_i a_i (\rho_i a_i + \rho_l a_l) (\rho_i a_i q_i + \rho_l a_l q_l) h_i}{(\rho_i a_i + \rho_l a_l) \Delta_{il} p + a_i (\rho_i a_i + \rho_l a_l)^2 - \rho_l a_l (\rho_i a_i + \rho_l a_l) \Delta_{il} q \cdot M} \right\} \right\} \delta_{il} \quad (A8) \\
& - M^2 \sum_{i \in v(i)} \frac{\rho_i a_i \rho_l a_l \Delta_{il} p q_i \Delta_{il} q + \rho_i a_i (\rho_i a_i q_i + \rho_l a_l q_l) (q_i \Delta_{il} p + a_i \rho_l a_l \Delta_{il} q)}{(\rho_i a_i + \rho_l a_l) \Delta_{il} p + a_i (\rho_i a_i + \rho_l a_l)^2 - \rho_l a_l (\rho_i a_i + \rho_l a_l) \Delta_{il} q \cdot M} \delta_{il} \\
& - M^3 \sum_{i \in v(i)} \frac{\rho_i a_i \rho_l a_l q_i (\rho_i a_i q_i + \rho_l a_l q_l) \Delta_{il} q}{(\rho_i a_i + \rho_l a_l) \Delta_{il} p + a_i (\rho_i a_i + \rho_l a_l)^2 - \rho_l a_l (\rho_i a_i + \rho_l a_l) \Delta_{il} q \cdot M} \delta_{il} = 0.
\end{aligned}$$

APPENDIX B

B.1 | Algorithm for 2D AM-HLLC-P

γ = ratio of specific heats

Left states:

ρ_L = density of i th cell

u_L = velocity component in the x direction of i th cell

v_L = velocity component in the y direction of i th cell

p_L = pressure of i th cell

$c_L = \sqrt{\gamma p_L / \rho_L}$

$e_L = p_L / \rho_L / (\gamma - 1) + \frac{1}{2} (u_L^2 + v_L^2)$

$h_L = e_L + p_L / \rho_L$

$q_L = u_L \cdot n_x + v_L \cdot n_y$

Right states:

ρ_R = density of $(i+1)$ th cell

u_R = velocity component in the x direction of $(i+1)$ th cell

v_R = velocity component in the y direction of $(i+1)$ th cell

p_R = pressure of $(i+1)$ th cell

$c_R = \sqrt{\gamma p_R / \rho_R}$

$e_R = p_R / \rho_R / (\gamma - 1) + \frac{1}{2} (u_R^2 + v_R^2)$

$h_R = e_R + p_R / \rho_R$

$q_R = u_R \cdot n_x + v_R \cdot n_y$

Roe averaged states:

$r = \sqrt{\rho_R / \rho_L}$

$\hat{u} = (u_L + r \cdot u_R) / (1 + r)$

$\hat{v} = (v_L + r \cdot v_R) / (1 + r)$

$\hat{h} = (h_L + r \cdot h_R) / (1 + r)$

$\hat{c} = \sqrt{(\gamma - 1) \cdot (\hat{h} - 0.5 \cdot \hat{u} \cdot \hat{u} - 0.5 \cdot \hat{v} \cdot \hat{v})}$

$\hat{q} = (q_L + r \cdot q_R) / (1 + r)$

$\hat{M} = \hat{q} / \hat{c}$

Wavespeeds:

$S_L = \min(q_L - c_L, q_R - c_R)$

$S_R = \max(q_L + c_L, q_R + c_R)$

$\alpha_L = \rho_L (S_L - q_L)$

$\alpha_R = \rho_R (S_R - q_R)$

$S^* = (\alpha_R q_R - \alpha_L q_L + p_L - p_R) / (\alpha_R - \alpha_L)$

Mach correction parameter:

$M_{LR} = \max \left(\sqrt{u_L \cdot u_L + v_L \cdot v_L} / c_L, \sqrt{u_R \cdot u_R + v_R \cdot v_R} / c_R \right)$

$\theta = \min(M_{LR}, 1.0)$

States in the star region:

$\rho_L^* = \alpha_L / (S_L - S^*)$

$\rho_R^* = \alpha_R / (S_R - S^*)$

$e_L^* = e_L + (S^* - q_L) \cdot (S^* + p_L / \alpha_L)$

$e_R^* = e_R + (S^* - q_R) \cdot (S^* + p_R / \alpha_R)$

$p^* = (\alpha_R \cdot p_L - \alpha_L \cdot p_R - \alpha_L \cdot \alpha_R \cdot (q_L - q_R)) / (\alpha_R - \alpha_L)$

$p^{**} = \theta \cdot p^* + (1 - \theta) \cdot 0.5 \cdot (p_L + p_R)$

$p^{***} = f \cdot p^{**} + (1 - f) \cdot p^*$

Pressure dissipative term:

$FluxP(1) = (f - 1) S_L S_R / (S_R - S_L) (p_R - p_L) / \hat{c} / \hat{c} / (1 + |\hat{M}|)$

$FluxP(2) = (f - 1) S_L S_R / (S_R - S_L) (p_R - p_L) / \hat{c} / \hat{c} / (1 + |\hat{M}|) \cdot \hat{u}$

$FluxP(3) = (f - 1) S_L S_R / (S_R - S_L) (p_R - p_L) / \hat{c} / \hat{c} / (1 + |\hat{M}|) \cdot \hat{v}$

$FluxP(4) = (f - 1) S_L S_R / (S_R - S_L) (p_R - p_L) / \hat{c} / \hat{c} / (1 + |\hat{M}|) \cdot 0.5 \cdot (\hat{u} \cdot \hat{u} + \hat{v} \cdot \hat{v})$

Left flux:

$FluxL(1) = \rho_L q_L$

$FluxL(2) = \rho_L q_L u_L + n_x p_L$

$FluxL(3) = \rho_L q_L v_L + n_y p_L$

$FluxL(4) = \rho_L q_L h_L$

Right flux:

$FluxR(1) = \rho_R q_R$

$FluxR(2) = \rho_R q_R u_R + n_x p_R$

$FluxR(3) = \rho_R q_R v_R + n_y p_R$

$FluxR(4) = \rho_R q_R h_R$

Flux at the left star region:

$FluxLS(1) = \rho_L^* S^*$

$FluxLS(2) = \rho_L^* S^* (u_L + n_x (S^* - q_L)) + n_x \cdot p^{***}$

$$FluxLS(3) = \rho_L^* S^* (v_L + n_y(S^* - q_L)) + n_y \cdot p^{***}$$

$$FluxLS(4) = S^* (\rho_L^* e_L^* + p^*)$$

Flux at the right star region:

$$FluxRS(1) = \rho_R^* S^*$$

$$FluxRS(2) = \rho_R^* S^* (u_R + n_x(S^* - q_R)) + n_x \cdot p^{***}$$

$$FluxRS(3) = \rho_R^* S^* (v_R + n_y(S^* - q_R)) + n_y \cdot p^{***}$$

$$FluxRS(4) = S^* (\rho_R^* e_R^* + p^*)$$

Total Flux:

$$\text{if}(S_L \geq 0)$$

$$Flux = FluxL$$

$$\text{if}(S_L \leq 0 \ \&\& \ S^* \geq 0)$$

$$Flux = FluxLS + FluxP$$

$$\text{if}(S^* \leq 0 \ \&\& \ S_R \geq 0)$$

$$Flux = FluxRS + FluxP$$

$$\text{if}(S_R \leq 0)$$

$$Flux = FluxR$$